# On the *p*H-dependent export of anthropogenic alkalinity in pore water through soil: Implications for enhanced rock weathering

Jacob S. Jordan[1], Mohammad Afzal Shadab[2], Valentina Prigiobbe[3], Yoshiki Kanzaki[4], Noah Planavsky[5], and Christopher T. Reinhard[4]

[1]Mati Carbon PBC, Houston TX, 77019
[2]Princeton University Department of Civil and Environmental Engineering, E209A Engineering Quadrangle Princeton, NJ 08544
[3]University of Padua, Department of Geosciences, Via Gradenigo 6, 35131 Padua (Italy)
[4]Georgia Institute of Technology School of Earth and Atmospheric Sciences, 311 Ferst Dr, Atlanta, GA 30332
[5]Yale Center for Natural Carbon Capture, PO Box 208109, New Haven CT 06520

## Abstract

Enhanced rock weathering (ERW) is a highly scalable carbon dioxide removal (CDR) strategy. In ERW deployments, pulverized mineral feedstock is spread on agricultural or managed lands. Upon the dissolution or weathering of the feedstock while exposed to the elements, cations are released, altering the charge balance of the pore water in the soil. The introduction of the divalent cations calcium ($Ca^{2+}$) and magnesium ($Mg^{2+}$) catalyzes the conversion of $CO_2$ to dissolved inorganic carbon (DIC), principally bicarbonate ($HCO_3^-$). The efficacy of ERW hinges on the maintenance and export of $HCO_3^-$ through the soil. To explore the mechanistic underpinnings of ERW, we develop a theoretical framework for the *p*H-dependent adsorption and desorption of cation solutes onto charged mineral surfaces in a porous medium. We develop a theory for the solution of the Riemann problem for a one-dimensional, quasi-linear $2 \times 2$ system of conservation laws for the transport of $Ca^{2+}$ and $Mg^{2+}$. The system is strictly hyperbolic, with the full *p*H-dependent system being non-genuinely nonlinear due to the non-convex, competitive Langmuir-type isotherms governing adsorption of $Ca^{2+}$ and $Mg^{2+}$. We present the structure of the eight fundamental solutions to the Riemann problem which are comprised of elementary and compound solute waves. Where alkaline solutions infiltrate acidic solutions in the pore water, compound reaction waves may arise. Such waves are always composed of fast-moving solute fronts and a slower-moving shock where $Ca^{2+}$ and $Mg^{2+}$ compete with hydrogen ion (or proton, $H^+$) for adsorption onto charged surface sites. The solutions to the Riemann problem presented here help interpret measurements from column experiments run to examine the efficiency of ERW and the general transport alkalinity in soils.

## 1 Introduction

It is widely accepted that limiting global warming since the start of the industrial revolution to under 2°C requires aggressive decarbonization and carbon dioxide removal (CDR) from Earth's atmosphere (IPCC, 2022). To this aim, it is commonly suggested that sustained CDR on the order of 1-10 gigatons of carbon dioxide ($CO_2$) will be required (National Academies of Sciences, Engineering, and Medicine, 2019; Fuss et al., 2018; Minx et al., 2018). One CDR approach that has garnered considerable interest is enhanced rock weathering (ERW). At ERW deployments, pulverized mineral feedstock is spread on agricultural or managed lands (Vienne et al., 2022; Guo et al., 2023; Beerling et al., 2024; Skov et al., 2024; Kantzas et al., 2025). Upon the dissolution of the mineral feedstock, cations principally calcium ($Ca^{2+}$) and magnesium ($Mg^{2+}$) are released, mobilizing alkalinity in the soil pore water (Hartmann et al., 2013; Strefler et al., 2018; Beerling et al., 2020). This process enhances the conversion of atmospheric $CO_2$ to dissolved inorganic carbon (e.g., $HCO_3^-$ and $CO_3^{2-}$) in the soil column. An illustrative weathering reaction for augite, a pyroxene that acts as a major constituent building block of a mineral feedstock used in ERW, basalt, is

$$\mathrm{CO_2(aq)} + \mathrm{H_2O} \rightleftharpoons \mathrm{H_2CO_3} \tag{1a}$$

$$\begin{aligned}(\mathrm{Ca}_x\mathrm{Mg}_y\mathrm{Fe}_z)(\mathrm{Mg}_{y'}\mathrm{Fe}_{z'})\mathrm{Si_2O_6} + 4\mathrm{H_2CO_3} \longrightarrow\ & x\mathrm{Ca}^{2+} + (y+y')\mathrm{Mg}^{2+} \\ & + (z+z')\mathrm{Fe}^{2+} + 2\mathrm{SiO_2(am)} + 4\mathrm{HCO_3^-}. \end{aligned} \tag{1b}$$

For augite, $0.4 \leq x \leq 0.9$, $x + y + z = 1$ and $y' + z' = 1$. The leftmost site as written in the formula for augite ($Ca_xMg_yFe_z$) represents a distorted octahedral coordination primarily occupied by calcium. This site can accept other large cations, predominantly alkaline earth or alkali elements. The other site ($Mg_{y'}Fe_{z'}$) represents a smaller octahedral coordination that preferentially accepts transition metals, primarily $Mg^{2+}$ and $Fe^{2+}$ (Cameron and Papike, 1981). Here, the bicarbonate ion ($HCO_3^-$) produced by this process can then be transported through soils via pore water into rivers and aquifers. Ultimately, if bicarbonate reaches the ocean, it can be stored for timescales approaching $10^4$ years (Archer et al., 1997; Archer, 2005; Renforth and Henderson, 2017).

When evaluating monitoring, reporting, and verification (MRV) techniques of CDR pathways for the purpose of generating carbon credits, there is a tendency to track units of carbon through the system. For example, practitioners may attempt to directly measure aqueous $CO_2$ and $HCO_3^-$ fluxes (Clarkson et al., 2024). However, it is also useful to track the fate of the dissolved cations (i.e., $Ca^{2+}$ and $Mg^{2+}$) that are released during initial feedstock dissolution, because it is the maintenance of charge balance with these cations in soil pore water that can lead to bicarbonate production (Reershemius et al., 2023; Bijma et al., 2026). Therefore, in many cases it is the fate of these cations, rather than that of any particular dissolved carbon species, that is critical to understanding the amount and rate of CDR that occurs as a result of an ERW intervention (Suhrhoff et al., 2024; te Pas et al., 2024). However, there is not a robust theoretical framework that can help predict and interpret the behavior of dissolved inorganic carbon through soil under various alkalinity conditions (see Clarkson et al., 2024; Bijma et al., 2026, and references therein).

In this manuscript, we develop a theoretical framework to explore the dynamics of pore water charge balance after the mobilization of $Ca^{2+}$ and $Mg^{2+}$. We model the flow of solutes in the pore water through an idealized soil column, which is cast as a simple porous medium with charged mineral surfaces. In the porous medium, $Ca^{2+}$ and $Mg^{2+}$ compete with acidity (protons, $H^+$), to adsorb onto these charged surfaces. The adsorption of the cations removes them from the solution, thereby altering the charge of the pore water and causing a potential loss of CDR. When divalent cations are removed from solution via adsorption onto charged mineral surfaces, protons are released, acidifying the pore water and shifting the carbonate equilibrium toward $CO_2$ (e.g., Reershemius et al., 2023; Bijma et al., 2026). The net effect (using calcium as an example for the divalent cation) can be expressed as

$$\mathrm{Ca}^{2+}(\mathrm{aq}) + 2\mathrm{HCO_3^-} \rightleftharpoons \mathrm{Ca}_s^{2+} + 2\mathrm{CO_2(aq)} + 2\mathrm{H_2O}, \tag{2}$$

where the subscript ($s$) denotes cation removal from solution via surface adsorption. This reaction represents a partial or complete reversal of the CDR achieved during initial silicate dissolution, as bicarbonate is converted back into aqueous $CO_2$ (te Pas et al., 2024; Suhrhoff et al., 2024). Given the complex dynamics of the geochemical system, we seek to gain insight into the mechanistic exchange between protons and the divalent cations at charged mineral surfaces during pore water flow (see McNeece and Hesse, 2016a; Appelo, 1996). To this aim, we solved an initial value problem defined by two constant states separated by a single discontinuity, called the Riemann problem, of a $2 \times 2$ system of conservation laws describing the reactive transport of $Ca^{2+}$ and $Mg^{2+}$ dissolved in a solution in equilibrium with the atmosphere moving through a porous medium (see Prigiobbe et al., 2013a; McNeece and Hesse, 2016a,b). The implications of charge balance and $p$H-dependent adsorption are explored. This ultimately has implications for the timing of bicarbonate transport through soil and thus the rate at which carbon may be sequestered using ERW deployments as a CDR strategy (Clarkson et al., 2024; Bijma et al., 2026).

## 2 Basic theory

### 2.1 Equations of solute transport in a reactive porous medium

The conservation of solute mass is used to derive equations for solute transport along a porous column of soil. An incompressible fluid with unidirectional flow is assumed to be in the $x$ direction. As such, lateral variations in the solute concentration are small relative to the variation in the streamwise direction (+x direction). The dissolved solutes are denoted $c_i$ where $i$ can be any species of dissolved solute (e.g. $Ca^{2+}$, $Mg^{2+}$, $H^+$). The concentration of any solute $i$ adsorbed onto a mineral surface of the soil grains comprising the porous medium, defined as loading $z_i$, is assumed to be motionless. The concentration of solutes in the pore water and onto the charged surfaces affects the geochemical equilibria of the entire porous medium. The mass balance equation for the dissolved solute (Bear, 1972; Steefel and Lasaga, 1994) is given by

$$\frac{\partial}{\partial t}\phi c_i + \frac{\partial}{\partial x}\left(q c_i - \phi D \frac{\partial}{\partial x} c_i\right) = -\Gamma_i, \tag{3}$$

where $t$ is the time, $\phi$ is the porosity, $D$ is diffusion coefficient, and $q = \phi(x,t)v(x,t)$ with $v$ being the interstitial velocity of water. The term $\Gamma$ represents the mass transfer of solute from the fluid phase (i.e., pore water) to the solid phase (i.e., soil) due to adsorption. We assume that the soil comprising the lattice of the porous medium does not move relative to the flow of pore water. Additionally, we assume that there is no local dispersion or molecular diffusion of the solute once it is attached to the mineral substrate on the soil, and local equilibrium in the liquid phase subsists (Rhee and Amundson, 1972; Knapp, 1989). Thus, the conservation of mass for the solute adsorbed onto the soil matrix is

$$\frac{\partial}{\partial t}(1-\phi) z_i = \Gamma_i. \tag{4}$$

By inspection, it is clear that the adsorption of solute onto the soil mineral surface in Equation (4) balances the solute lost from the fluid in Equation (3).

Following Rhee et al. (1989) and Prigiobbe et al. (2012a), we non-dimensionalize the system using the characteristic variables defined as

$$x = Lx', \quad v = \bar{v}v', \quad c_i = c^* c_i', \quad z_i = z^* z_i', \quad D = D^* D', \quad \Gamma_i = \Gamma^* \Gamma_i', \quad t = \frac{L}{\bar{v}} t'. \tag{5}$$

Here, asterisks, $*$, represent the characteristic scale for the corresponding quantity, while primes, $'$, denote the corresponding dimensionless variable. The variables $L$ and $\bar{v}$ are the length and the characteristic scale for bulk pore water velocity, respectively. The dimensionless system of the solute transport equations writes

$$\frac{\partial}{\partial t'}\phi c_i' + \frac{\partial}{\partial x'}\phi c_i' - \mathrm{Pe}^{-1}\left[\frac{\partial}{\partial x'}\left(\phi D' \frac{\partial}{\partial x'} c_i'\right)\right] = -\mathrm{Da}\, \Gamma_i', \tag{6a}$$

$$\frac{\partial}{\partial t'}(1-\phi) z_i' = \mathrm{Da}\, \Gamma_i', \tag{6b}$$

where Pe is the Péclet number defined as the ratio between advective and diffusive transport timescale ($\mathrm{Pe} = \frac{D^*}{\bar{v}L}$) and Da is the dimensionless ratio commonly referred to as the Damköhler number,

$$\mathrm{Da} = \frac{\Gamma^* L}{c_i^* \bar{v}}. \tag{7}$$

The Damköhler number is conventionally defined as the ratio of the transport timescale to the reaction timescale, $\mathrm{Da} = \tau_{\text{transport}}/\tau_{\text{reaction}}$, where $\tau_{\text{reaction}}$ is typically set by a kinetic rate constant (e.g., Steefel and Lasaga, 1994). In the limit $\mathrm{Da} \gg 1$, reactions are fast relative to transport and local chemical equilibrium is attained. We note that regardless of the magnitude of Da, the source terms in Equations. (6a) and (6b) are equal and opposite, ensuring that the total mass of each solute species is conserved across the fluid and solid phases. In the analysis that follows, we take the local equilibrium limit ($\mathrm{Da} \to \infty$), which eliminates the need to specify an explicit kinetic rate law for adsorption.

## 2.2 General solute adsorption equation

To describe the adsorbed concentration of the solute onto the soil ($\Gamma_i$), we formulate a surface complexation model considering a solution containing competing cations, $\mathrm{S}_i^{n+}$, that react with a charged surface (Dzombak and Morel, 1990). In this formulation, we assumed the intrinsic equilibrium constant equal neglecting the terms containing electrostatic surface potentials (e.g. Sposito, 2004, 2008b). In this notation, the superscript $n$ represents the charge of the solute or proton in the pore water, and $i$ denotes the species of the charged cation. Following Prigiobbe et al. (2012a), the adsorption and desorption reactions at the pore water-soil interface are described by

$$\mathrm{X}^{-1/2} + \mathrm{S_i}^{n_i+} \rightleftharpoons \mathrm{XS}_i^{n_i-1/2}, \tag{8}$$

where $\mathrm{X}^{-1/2}$ represents a free reactive surface site on the soil surface. Neglecting electrostatic terms, the effective equilibrium constants are given as

$$K_i = \frac{\left\{\mathrm{XS}_i^{n_i-1/2}\right\}}{c_i \left\{\mathrm{X}^{-1/2}\right\}} \tag{9}$$

where $c_i$ corresponds to the concentrations of cations or protons. The total surface site balance, or "loading" is given by

$$Z_t = \left\{\mathrm{X}^{-1/2}\right\} + \sum_{i=1}^{k} \left\{\mathrm{XS}_i^{n_i-1/2}\right\}, \tag{10}$$

where $Z_t$ is the total concentration of reactive surface sites at the pore water-soil interface (Appelo, 1996). This includes unoccupied charged sites and all sites occupied by solutes or protons. Here, $Z_t$ is written from the "perspective" of the pore water, i.e., the concentration of charged sites on the soil particle interface is interpreted in terms of pore water volume within the soil, e.g., moles of charged sites per liter of pore water (mol $L^{-1}$ of solution) rather than moles per kilogram of solid soil (mol $kg^{-1}$ of soil).

Combining equations (9) and (10) the equilibrium concentration of all solutes and protons adsorbed onto the soil surface, $z_i$, is

$$z_i = \frac{c_i K_i Z_t}{1 + \sum_{i=1}^{k} c_i K_i}, \tag{11}$$

where $z_i$ is indeed $\sum_{i=1}^{k} \left\{ \mathrm{XS}_i^{n_i - 1/2} \right\}$ (e.g. Prigiobbe et al., 2013a; Appelo, 1996). In the simplest case where only one reactive solute is considered, Equation (11) simplifies to

$$z = \frac{c K Z_t}{1 + cK}, \tag{12}$$

which resembles the well-known equation of the Langmuir adsorption isotherm (Langmuir, 1918).

## 2.3 Competitive solute adsorption and the carbonate system

We begin a case study by taking equations (8) through (11) and explicitly specifying species $i \in \{\mathrm{Ca}^{2+}, \mathrm{Mg}^{2+}, \mathrm{H}^+\}$ so the loading term for adsorption onto soil surfaces can be directly written as,

$$Z_t = \left\{ \mathrm{X}^{-1/2} \right\} + \left\{ \mathrm{XH}^{+1/2} \right\} + \left\{ \mathrm{XCa}^{+3/2} \right\} + \left\{ \mathrm{XMg}^{+3/2} \right\}. \tag{13}$$

In this work, $Z_t$ is akin to a simplified cation exchange capacity (CEC) for the low-concentration pore water regime in the soil column.

Under the geochemical conditions of interest, the solution speciation consists of the dissociation of water and carbonic acid,

$$\mathrm{H_2O} \rightleftharpoons \mathrm{OH}^- + \mathrm{H}^+, \tag{14}$$

$$\mathrm{CO_2(aq)} + \mathrm{H_2O} \rightleftharpoons \mathrm{HCO_3}^- + \mathrm{H}^+. \tag{15}$$

Assuming that the activity of water and the activity coefficients of the solutes are unity (Stumm and Morgan, 1996a), the equilibrium constants of Equations (14) and (15) are

$$K_w = [\mathrm{H}^+][\mathrm{OH}^-] = c_{\mathrm{H}} c_{\mathrm{OH}}. \tag{16}$$

and

$$K_1 = \frac{[\mathrm{HCO_3^-}][\mathrm{H}^+]}{[\mathrm{CO_2}]} = \frac{c_{\mathrm{HCO_3}} c_{\mathrm{H}}}{c_{\mathrm{CO_2}}}, \tag{17}$$

respectively. The concentration of $CO_2$ in the soil may vary significantly by location (Amundson et al., 1998). If we assume that the partial pressure of $CO_2$, $pCO_2$, remains approximately constant in an open system and that dissociation kinetics are fast compared to any relevant transport timescale (Drever,

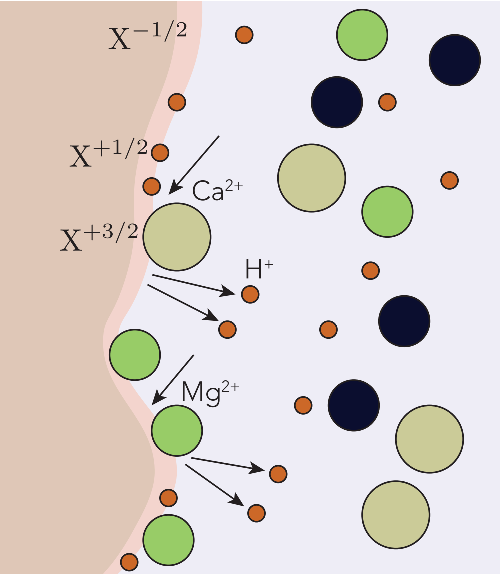

Figure 1: A schematic diagram showing the competitive adsorption of $H^+$, $Ca^{2+}$, and $Mg^{2+}$ onto a charged solid surface in the soil (see equation 13). The relative sizes of the cations are scaled with respect to their ionic radii.

1997), we can determine the dissolved $CO_2$ in the soil-pore water solution using the formula for the equilibrium constant of carbonate systems,

$$[\mathrm{H_2CO_3}] = \frac{p\mathrm{CO_2}(z)}{h_c} = c_{\mathrm{CO_2}}. \tag{18}$$

Here, $h_c$ is Henry's constant ($h_c \approx 29$ $CO_2$ in water at 25 °C with units of (L·atm)/mol) and $z$ is depth. Given $pCO_2$ for the soil, Equation (18) may be used in (17) instead of $c_{CO_2}$. Here we note that $pCO_2(z)$ may vary with depth, as the soil-atmosphere interface constitutes an open system for carbonic acid speciation relationships. For depths below the upper boundary layer of the soil, we assume that $pCO_2$ is approximately constant. This is done for analytical clarity. However, future iterations of this modeling exercise could include calculations for $pCO_2$ as a function of depth (see Cerling, 1984; Amundson et al., 1998).

In this analysis, we assume the aqueous phase is charge balanced, and the electroneutrality condition is given by

$$c_a + c_{\mathrm{OH}} + c_{\mathrm{HCO_3}} = c_{\mathrm{H}} + 2c_{\mathrm{Ca}} + 2c_{\mathrm{Mg}}. \tag{19}$$

Here, the negatively charged ions are on the left-hand side, while the positively charged solutes and protons are balanced on the right-hand side. The first term on the left-hand side, $c_a$, is a yet-to-be-defined anion concentration in the pore fluid. We define this anion concentration as

$$c_a = c_{\tilde{\mathrm{N}}} - c_{\mathrm{Na}}, \tag{20}$$

where $c_{\tilde{N}}$ is the concentration of a conservative monovalent anion (e.g., $Cl^-$) that does not participate in adsorption or carbonate equilibria (Stumm and Morgan, 1996b; Drever, 1997). We choose chloride

Table 1: Model parameters for the example case study at 25°C. Adsorption constants, $K_i$, assume a solid surface consisting of ferrihydrite (hydrous ferric oxide, HFO).

| **Parameter** | **Symbol** | **Literature** | **This study** |
|---|---|---|---|
| *Adsorption constants* ($\log_{10} K_i$) | | | |
| $H^+$ adsorption constant | $K_{\mathrm{H}}$ | $8.7^a$ | 8 |
| $K^+$ adsorption constant | $K_{\mathrm{K}}$ | $-0.38^b$ | – |
| $Na^+$ adsorption constant | $K_{\mathrm{Na}}$ | $-0.38^c$ | – |
| $Ca^{2+}$ adsorption constant | $K_{\mathrm{Ca}}$ | $3.10^c$ | 3 |
| $Mg^{2+}$ adsorption constant | $K_{\mathrm{Mg}}$ | $4.33^c$ | 4 |
| *Pore water and transport parameters* | | | |
| Total surface site concentration | $Z_t$ | | $10^{-2}$ mol $L^{-1}$ |
| Porosity ratio | $\varphi = (1-\phi)/\phi$ | | 4 |
| Partial pressure of $CO_2$ | $pCO_2$ | | $10^{-3.5}$ atm |
| Henry's constant | $h_c$ | | 29 (L·atm)/mol |
| Dissolved $CO_2$ concentration | $c_{\mathrm{CO_2}}$ | | $pCO_2/h_c$ |
| First dissociation constant of carbonic acid | $K_1$ | | $10^{-6}$ |
| Water dissociation constant | $K_w$ | | $10^{-14}$ |
| Strong ion difference | $c_a$ | | $2Z_t = 2 \times 10^{-2}$ mol $L^{-1}$ |

[a] van Beinum et al. (2005), [b] Rahnemaie et al. (2006b), [c] Rahnemaie et al. (2006a).

($Cl^-$) and $Na^+$ as the balancing species for two reasons: (i) their abundance in rainwater and natural salts (Drever, 1997), and (ii) sodium's abundance in enhanced weathering feedstocks such as basalt (e.g., Hartmann et al., 2013). Moreover, sodium's participation in the charge balance (Equation 19) suggests that $Na^+$ contributes to the conversion of $H_2CO_3$ to $HCO_3^-$ and, therefore, the drawdown of $CO_2$ in natural systems (Stumm and Morgan, 1996b). The reader may notice that neither $Cl^-$ nor $Na^+$ appear in the total surface balance or equilibrium loading isosurfaces. This is because the values for $K_{\mathrm{Na}}$ and $K_{\mathrm{Cl}}$ are orders of magnitude smaller than those of $H^+$, $Ca^{2+}$, and $Mg^{2+}$ (Rahnemaie et al., 2006a,b). Therefore, we assume that $Cl^-$ and $Na^+$ instantaneously balance the charge of the pore water on timescales fast relative to the adsorption of ions described in Equations (B.1a) through (B.1c).

Next, we combine Equations (17) through (19). Now, the expression for proton concentration can be rewritten as the physically relevant (positive) solution to the following quadratic

$$c_{\mathrm{H}} = \frac{c_{\mathrm{a}} - 2c_{\mathrm{Ca}} - 2c_{\mathrm{Mg}} \pm \sqrt{4\left(c_{\mathrm{Ca}}^2 + c_{\mathrm{Mg}}^2 - c_a\left(c_{\mathrm{Ca}} + c_{\mathrm{Mg}}\right) + 2c_{\mathrm{Ca}}c_{\mathrm{Mg}} + c_{\mathrm{CO_2}}K_1 + K_w\right) + c_a^2}}{2}. \tag{21}$$

It is worth noting here that the method presented above is agnostic to the various sources of acidity in the pore water. As such, the method may easily be extended to account for more sources of acidity (various strong acids derived from crop amendments, organic acids, etc. (Taylor et al., 2021; Vicca et al., 2022)).

To illustrate the theoretical framework, we carry the analysis through a specific example case. The model parameters are summarized in Table 1. The adsorption constants are rounded from the ferrihydrite surface complexation data in the literature, and the remaining parameters define the pore water chemistry and surface site density. Due to low $K$ values for potassium ($K^+$) and sodium ($Na^+$), we focus our adsorption study on $H^+$, $Ca^{2+}$, and $Mg^{2+}$. The partial pressure of $CO_2$ is set to $p\mathrm{CO}_2 = 10^{-3.5}$ atm, corresponding to near-atmospheric conditions at the soil surface or in a well-ventilated shallow soil profile (Cerling, 1984; Amundson et al., 1998). The total surface site concentration, $Z_t = 10^{-2}$ mol L$^{-1}$, represents a low cation exchange capacity consistent with weathered or coarse-textured soils (Sposito, 2008a). The strong ion difference is set to $c_a = 2Z_t = 2 \times 10^{-2}$ mol L$^{-1}$, which imposes a significant excess of conservative anions over sodium. In the acidic limit of composition space (i.e., when divalent cation concentrations are negligible), this value of $c_a$ yields a pore water $p$H of approximately 1.7, comparable to moderately concentrated acid mine drainage (Blowes et al., 1994; Nordstrom, 2011). In the alkaline region, where divalent cation concentrations are sufficient to consume most of the excess acidity via charge balance (e.g., $c_{\mathrm{Ca}} = c_{\mathrm{Mg}} \approx 5 \times 10^{-3}$ mol L$^{-1}$), the pore water $p$H rises to approximately 5.5, consistent with weathered agricultural soils subject to ammonium-based fertilizer amendments or moderate acid deposition (Drever, 1997; Taylor et al., 2021). For reference, typical acid rain delivers $c_{\mathrm{H}} \sim 10^{-4}$ mol L$^{-1}$ ($p\mathrm{H} \approx 4$), whereas acid mine drainage systems routinely exhibit sulfate concentrations of $10^{-2}$–$10^{-1}$ mol L$^{-1}$ and $p$H values of 2–4 (Nordstrom, 2011; Jurjovec et al., 2002). The value of $c_a$ adopted here therefore spans the transition between these regimes.

We emphasize that the choice of $c_a$ and $p\mathrm{CO}_2$ exerts a first-order control on the structure of the Riemann solutions that we present below (Section 3). In particular, the balance between strong acid and carbonic acid contributions to the pore water governs whether silicate dissolution generates bicarbonate alkalinity and therefore sequesters atmospheric $CO_2$ or merely neutralizes pre-existing acidity without net carbon removal (Hamilton et al., 2007; Hartmann et al., 2013). In acidic tropical soils where strong acids dominate the weathering budget, measured $CO_2$ removal via enhanced rock weathering can be negligible despite substantial mineral dissolution (Holden et al., 2024). Conversely, in systems where strong acid concentrations are low relative to carbonic acid, either naturally or following progressive neutralization by prior weathering, the same dissolution reactions yield significant alkalinity export and carbon sequestration (Taylor et al., 2021; Hamilton et al., 2007). The example parameters adopted here place the system in a regime where both strong acid and carbonic acid weathering pathways are active, and the resulting wave structures reflect this coexistence. The sensitivity of the solution morphology to $c_a$ and $p\mathrm{CO}_2$ is explored further in Section 4.

## 2.4 Non-convex loading isosurfaces with acidic and alkaline regions

The loading term, $Z_t$, is chosen as the characteristic scale $z^*$ in equation (5) (Prigiobbe et al., 2012a). This scale is applied to the values $K_i$ for all solutes considered in the model ($i \in \{\mathrm{Ca}^{2+}, \mathrm{Mg}^{2+}, \mathrm{H}^+\}$) and the equilibrium constants and concentrations that play a role in the carbonic acid system, so

$$K_{\mathrm{i}} = Z_t K'_{\mathrm{i}}, \quad K_1 = Z_t K'_1, \quad K_{\mathrm{w}} = Z_t K'_{\mathrm{w}} \quad c_{\mathrm{CO}_2} = Z_t c'_{\mathrm{CO}_2}, \quad \text{and} \quad c_{\mathrm{a}} = Z_t c'_{\mathrm{a}}. \tag{22}$$

After scaling using equations (5) and (22), equation (21) is written in a dimensionless form. For the sake of clarity, the scaling does not change the structure of equation (21) and the expression of $c'_{\mathrm{H}}$ is identical to that of $c_{\mathrm{H}}$ if the prime notation is dropped.

The expressions for the loading isosurfaces are cast in dimensionless terms as

$$z'_{\mathrm{Ca}}(c'_{\mathrm{Ca}}, c'_{\mathrm{Mg}}) = \varphi \left( \frac{c'_{\mathrm{Ca}} K'_{\mathrm{Ca}}}{1 + c'_{\mathrm{H}}(c'_{\mathrm{Ca}}, c'_{\mathrm{Mg}}) K'_{\mathrm{H}} + c'_{\mathrm{Ca}} K'_{\mathrm{Ca}} + c'_{\mathrm{Mg}} K'_{\mathrm{Mg}}} \right), \tag{23a}$$

$$z'_{\mathrm{Mg}}(c'_{\mathrm{Ca}}, c'_{\mathrm{Mg}}) = \varphi \left( \frac{c'_{\mathrm{Mg}} K'_{\mathrm{Mg}}}{1 + c'_{\mathrm{H}}(c'_{\mathrm{Ca}}, c'_{\mathrm{Mg}}) K'_{\mathrm{H}} + c'_{\mathrm{Ca}} K'_{\mathrm{Ca}} + c'_{\mathrm{Mg}} K'_{\mathrm{Mg}}} \right), \tag{23b}$$

$$z'_{\mathrm{H}}(c'_{\mathrm{Ca}}, c'_{\mathrm{Mg}}) = \varphi \left( \frac{c'_{\mathrm{H}}(c'_{\mathrm{Ca}}, c'_{\mathrm{Mg}}) K'_{\mathrm{Ca}}}{1 + c'_{\mathrm{H}}(c'_{\mathrm{Ca}}, c'_{\mathrm{Mg}}) K'_{\mathrm{H}} + c'_{\mathrm{Ca}} K'_{\mathrm{Ca}} + c'_{\mathrm{Mg}} K'_{\mathrm{Mg}}} \right), \tag{23c}$$

where

$$\varphi = \phi/(1-\phi), \tag{24}$$

(see Equation C.2). Henceforth, we drop prime-notation while developing the theory presented in this manuscript. For the remainder of this work, all equations are dimensionless unless noted otherwise. See equations (B.1a–B.1c) in Appendix B for the dimensional formulation of the loading isosurfaces.

Figure 2 shows the loading isosurfaces normalized with respect to $\varphi$ and reported as a function of normalized $Ca^{2+}$ and $Mg^{2+}$ concentrations. Here, all the prime signs have been dropped for brevity.

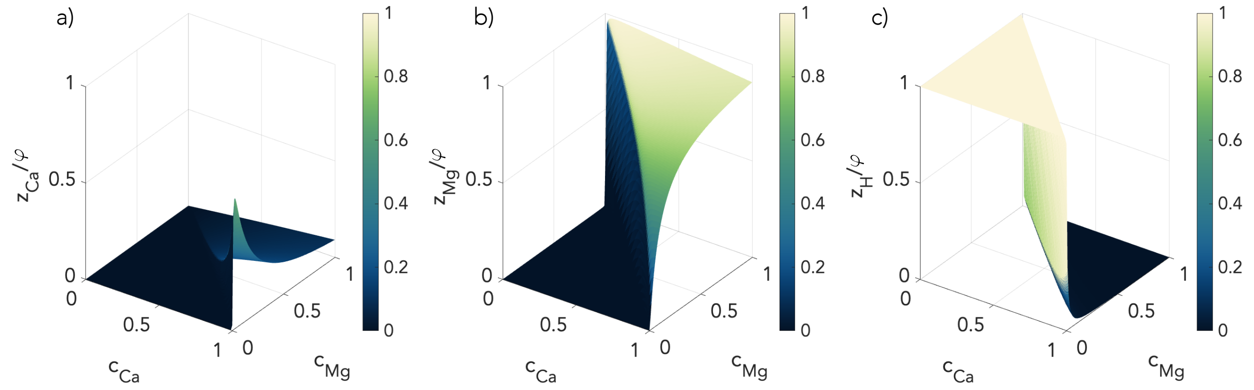

Figure 2: Loading isosurfaces normalized with respect to $\varphi$ that illustrate the equilibrium loading of $H^+$, $Ca^{2+}$, and $Mg^{2+}$ onto charged soil surfaces in the porous medium. These competitive Langmuir-type isotherms are non-convex and the strong adsorption of protons onto soil sites at low $p$H drives behaviors for the solutions to the Riemann problem.

Throughout the remainder of this work, we find it convenient to refer to the cation-rich region of $c_{\mathrm{Ca}} - c_{\mathrm{Mg}}$ space as "alkaline" (elevated plateaus in Figure 2a-b), and the proton-rich region as "acidic" (elevated plateaus in Figure 2c). In the acidic region of $c_{\mathrm{Ca}} - c_{\mathrm{Mg}}$ space, protons dominate adsorption onto the charged surface sites. This is because $K_{\mathrm{H}} \gg K_{\mathrm{Ca,Mg}}$ and therefore proton adsorption is favored over that of calcium and magnesium. In the alkaline region of $c_{\mathrm{Ca}} - c_{\mathrm{Mg}}$ space, where the concentration of protons is negligible with respect of those of the cations, the adsorption of $Ca^{2+}$, and $Mg^{2+}$ onto the charged sites dominates. The shapes of the non-convex loading isosurfaces are highly sigmoidal in nature (McNeece and Hesse, 2016a). The inflection point of the loading isosurfaces has a strong influence on the behavior of cation transport when pore water from the alkaline and acidic regions mix as we will show in this paper below. The isosurface inflection point is circumneutral through the $c_{\text{Ca}} - c_{\text{Mg}}$ phase-space and is the source of many novel chromatographic behaviors of $p$H-dependent systems (Prigiobbe et al., 2013b, 2012b).

## 2.5 Self-similar solutions to the dimensionless conservation laws in an advection dominated transport regime

Considering an incompressible and isothermal fluid, and assuming advection dominated transport regime ($\text{Pe} \gg 1$), the dimensionless coupled solute transport equations (Equations 6b and 6a) are hyperbolic differential equations,

$$(1 + \nabla_c \mathbf{z}(\mathbf{c})) \frac{\partial c_{\text{Ca}}}{\partial t} + \frac{\partial c_{\text{Ca}}}{\partial x} = 0, \quad x \in \mathbb{R},\ t > 0, \tag{25a}$$

$$(1 + \nabla_c \mathbf{z}(\mathbf{c})) \frac{\partial c_{\text{Mg}}}{\partial t} + \frac{\partial c_{\text{Mg}}}{\partial x} = 0, \quad x \in \mathbb{R},\ t > 0, \tag{25b}$$

where $\nabla_c \mathbf{z}$ is the adsorption gradient given by a $2 \times 2$ matrix for $\mathbf{z} = [z_{\text{Ca}}, z_{\text{Mg}}]^T$ differentiated with respect to $\mathbf{c} = [c_{\text{Ca}}, c_{\text{Mg}}]^T$. This system is similar to that considered by Valocchi et al. (1981), Charbeneau (1988a), Lake et al. (2002), Prigiobbe et al. (2013b), and McNeece et al. (2018) but the isosurfaces are different.

We solve the "Riemann Problem" which considers the initial condition characterized by a jump-discontinuity separating two constant states. The mathematical construct of such a jump discontinuity is analogous to column flooding experiments commonly performed in laboratories, where a chromatographic column stabilized with a solution (right constant state) is then injected with another solution with different composition (left constant state). Column flow-through configurations of this kind are widely employed in studies of silicate dissolution for enhanced rock weathering and carbon mineralization (Renforth et al., 2015; Vienne et al., 2022; Khalidy and Santos, 2024; Kelland et al., 2020), as well as in acid mine drainage remediation where acid fronts displace alkaline pore waters through reactive media (Blowes et al., 1994; Jurjovec et al., 2002). The piecewise constant initial condition for the conserved quantities in $\mathbf{c}$ is written:

$$\mathbf{c}(x, t = 0) = \begin{cases} \mathbf{c}_l & \text{for } x < 0, \\ \mathbf{c}_r & \text{for } x > 0. \end{cases} \tag{26}$$

The superscripts $l$ and $r$ indicate "left" and "right" initial states. We assume that the flow of pore water and solute is primarily driven in the positive direction. Therefore, the convention is that the fluid flows along the directional axis from "left" to "right". At $t = 0$, the jump-discontinuity in the concentration field is located at zero in the coordinate system. Figure 3 shows an experimental set-up with a chromatographic column (panels a and b) where a jump-discontinuity in solute concentration is applied. In a simple chromatographic column experiment, a column is equilibrated with the "right state" $\mathbf{c}_r$ and then the "left state" $\mathbf{c}_l$ is pumped through the chromatographic column. The theory presented in this manuscript is analogous to an idealized chromatographic column with a constant bulk pore water velocity $\bar{v}$.

The weak solution of the Riemann problem for hyperbolic systems is invariant under a uniform stretching transformation of the native variables (i.e. $\bar{x} = e^{\alpha} x$, $\bar{t} = e^{\alpha} t$); i.e., the solutions to the coupled equations (25a) and (25b) do not change shape as they evolve in the space-time plane (Lax,

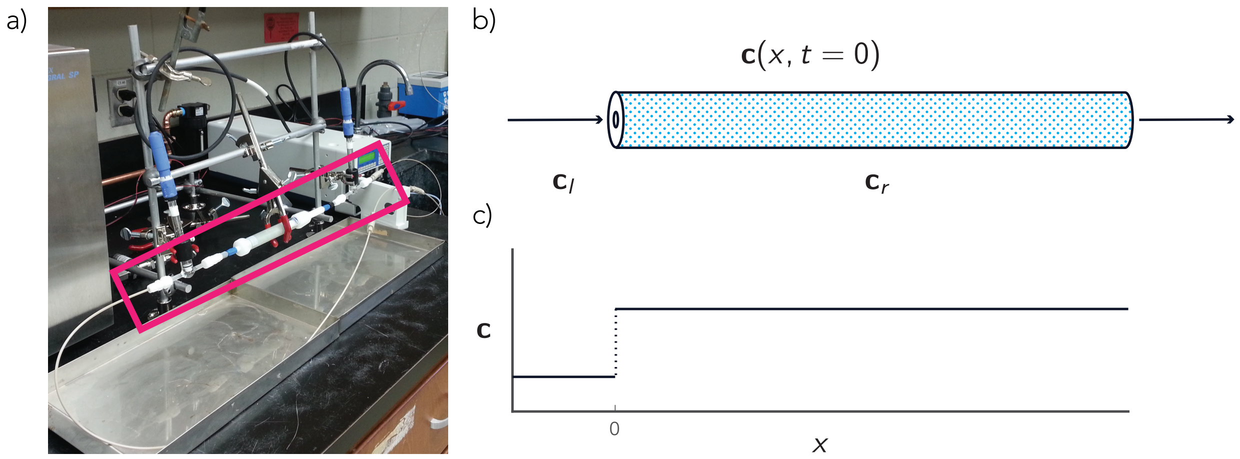

Figure 3: a, b) Photo and schematic of a chromatographic column to test reactive transport problems. c) Schematic diagram of the so-called "Riemann problem" initial conditions given in Equation 26.

1957). Therefore, we seek a so-called "similarity variable," $\eta$, to recast the system of partial differential equations into a system of ordinary differential (ODEs) equations,

$$\eta := \frac{x}{t}. \tag{27}$$

Using equation (27) and applying the linear transformation, we derive a $2 \times 2$ system of ODEs that can be solved as a nonlinear eigenvalue problem,

$$(\nabla_c \mathbf{z}(\mathbf{c}) - \theta_p \mathbf{I}) \frac{d\mathbf{c}}{d\eta} = 0. \tag{28}$$

Here, $\theta_p$ are the eigenvalues for the $p^{th}$ solution to Equation (28). Because Equation (28) is a $2 \times 2$ system, there are two eigenvalues $p \in \{1, 2\}$. The two solutions to the eigenvalue problem yield two elementary waves, $\mathcal{W}_p$, that emanate from the jump in the initial condition of the Riemann problem referred to as Riemann initial condition. In the context of multicomponent chromatography, each elementary wave corresponds to a coherent composition variation in which all species concentrations change in lock-step as the wave propagates (Helfferich and Klein, 1970; Helfferich, 1993). The physical interpretation of these waves is reactive fronts of solute flowing through the porous medium. In subsurface transport, each wave represents a reaction front across which the pore water composition transitions between two locally equilibrated states; for example, the displacement of calcium-rich pore water by an invading acidic solution produces distinct fronts whose speeds are governed by the buffering capacity of the exchange complex (Charbeneau, 1988b; Appelo, 1996; Venkatraman et al., 2014). The velocity of the reaction fronts, hereafter termed "wave speed," $v_p$, is given by a relationship with the eigenvalues $\theta_p$ provided in equation (28) as

$$v_p = \sigma_p^{-1} = \eta, \quad \text{where} \quad \theta_p = \sigma_p - 1, \text{ and } p \in \{1, 2\}. \tag{29}$$

As such, the term $\sigma_p$ describes the retardation of wave $\mathcal{W}_p$ normalized to the bulk pore water velocity, $\bar{v}$. Retardation arises because solute mass is partitioned between the mobile aqueous phase and the immobile adsorbed phase; a wave whose associated species are strongly sorbed ($K_i \gg 1$) is retarded significantly relative to the bulk flow, whereas a wave dominated by weakly sorbing species propagates near the pore water velocity (Helfferich and Klein, 1970; Charbeneau, 1988b). In the limiting case of a single non-interacting solute with linear isotherm, $\sigma_p$ reduces to the classical retardation factor $R = 1 + K_d$ familiar from contaminant hydrogeology (Bear, 1972).

We have chosen a convention such that the eigenvalues are ordered according to the speeds of the two waves, $\mathcal{W}_1$ and $\mathcal{W}_2$. As the two solute waves advance in space-time from the Riemann initial condition, they separate. The slower of the two, i.e., $\mathcal{W}_1$, is associated with the first characteristic field $\theta_1$. The faster of the two waves, $\mathcal{W}_2$, is associated with $\theta_2$ and advances in space-time more rapidly than $\mathcal{W}_1$. Therefore, the solute wavefronts separate "chromatographically" (Helfferich and Klein, 1970; Rhee and Amundson, 1972). To calculate the eigenvalues $\theta_p$ analytically, we obtain a characteristic polynomial of the Jacobian matrix for the full system and solve for its roots. The Jacobian matrix is given by, the first term in equation (28). This $2 \times 2$ matrix is obtained by substituting equation (21) into scaled expressions of the sorption isotherms.

The characteristic polynomial of the accumulation term in the eigenvalue problem is given by:

$$\theta_p^2 - \left(\frac{\partial z_{\mathrm{Ca}}}{\partial c_{\mathrm{Ca}}} + \frac{\partial z_{\mathrm{Ca}}}{\partial c_{\mathrm{Mg}}}\right)\theta_p + \left(\frac{\partial z_{\mathrm{Ca}}}{\partial c_{\mathrm{Ca}}}\frac{\partial z_{\mathrm{Mg}}}{\partial c_{\mathrm{Mg}}} - \frac{\partial z_{\mathrm{Ca}}}{\partial c_{\mathrm{Mg}}}\frac{\partial z_{\mathrm{Mg}}}{\partial c_{\mathrm{Ca}}}\right) = 0. \tag{30}$$

Solving the eigenvalue problem, the eigenvalues of (28) are,

$$\theta_1 = \frac{\left(\frac{\partial z_{\mathrm{Ca}}}{\partial c_{\mathrm{Ca}}} + \frac{\partial z_{\mathrm{Mg}}}{\partial c_{\mathrm{Mg}}}\right) - \sqrt{\varDelta}}{2}, \tag{31a}$$

$$\theta_2 = \frac{\left(\frac{\partial z_{\mathrm{Ca}}}{\partial c_{\mathrm{Ca}}} + \frac{\partial z_{\mathrm{Mg}}}{\partial c_{\mathrm{Mg}}}\right) + \sqrt{\varDelta}}{2}, \tag{31b}$$

with

$$\varDelta = \left(\frac{\partial z_{\mathrm{Ca}}}{\partial c_{\mathrm{Ca}}} + \frac{\partial z_{\mathrm{Mg}}}{\partial c_{\mathrm{Mg}}}\right)^2 - 4\left(\frac{\partial z_{\mathrm{Ca}}}{\partial c_{\mathrm{Ca}}}\frac{\partial z_{\mathrm{Mg}}}{\partial c_{\mathrm{Mg}}} - \frac{\partial z_{\mathrm{Ca}}}{\partial c_{\mathrm{Mg}}}\frac{\partial z_{\mathrm{Mg}}}{\partial c_{\mathrm{Ca}}}\right). \tag{32}$$

For each eigenvalue $\theta_1$ and $\theta_2$, we find the corresponding eigenvectors $\mathbf{r}_p$ to be

$$\mathbf{r}_p = \frac{d\mathbf{c}}{d\eta} = \begin{bmatrix} \frac{\partial z_{\mathrm{Ca}}}{\partial c_{\mathrm{Mg}}} \\ \theta_p - \frac{\partial z_{\mathrm{Ca}}}{\partial c_{\mathrm{Ca}}} \end{bmatrix}, \quad p \in \{1, 2\}. \tag{33}$$

Contours of each eigenvalue are shown in Figure 4.

## 3 Solution structure and the "hodograph plane"

The weak solution of the Riemann problem for a strictly hyperbolic system of $2 \times 2$ equations results in a combination of two waves. These two waves connect three distinct states of the system. It is conventional to order these waves according to their speed, so $\mathcal{W}_1$ is the so-called "slow wave"," and $\mathcal{W}_2$ is the "fast wave". The waves connect the left and right states from equation (26) with a middle state, $c_m$, yielding:

$$\mathbf{c}_l \xrightarrow{\mathcal{W}_1} \mathbf{c}_m \xrightarrow{\mathcal{W}_2} \mathbf{c}_r. \tag{34}$$

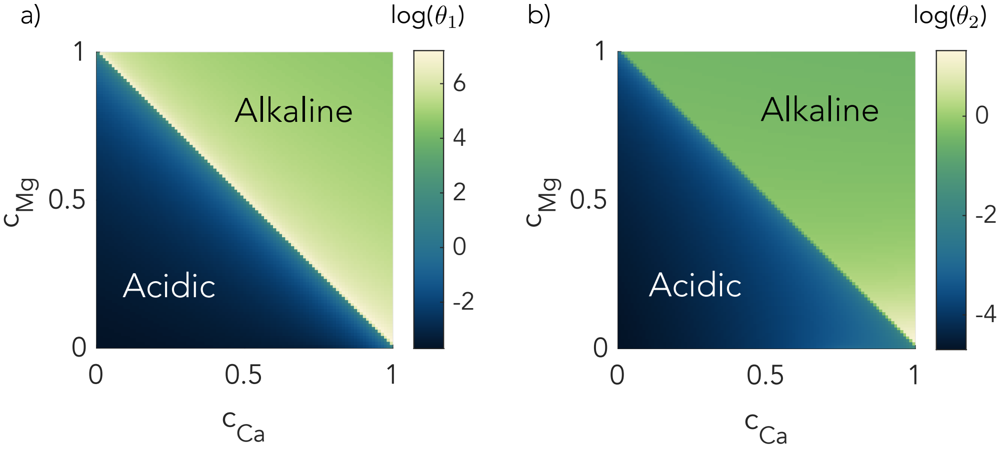

Figure 4: Eigenvalues, a) $\theta_1$ and b) $\theta_2$ for the case where the dimensional equilibrium constants for adsorption in the soil-pore water mixture are given in Table 1. For each characteristic field, the retardation of the associated reaction front is given by $\sigma_p = \theta_p - 1$ and $\sigma_p = 1/\bar{v}$. In the acidic region, protons dominate adsorption onto the charged surfaces of the soil (Figure 2). Because $K_{\mathrm{H}} \gg K_{\mathrm{Ca,Mg}}$ calcium and magnesium cannot compete with protons for adsorption. Thus, the retardation of cations is $\sim 0$ for both characteristic fields in this region of composition space. In the alkaline region of composition space, the pore water contains enough cations relative to protons that they are able to compete with for adsorption sites (Figure 2).

The full structure of the solution first requires obtaining the two waves and locating their intersection on the so-called "hodograph plane". The hodograph plane is defined as the space of conserved quantities– here $c_{\mathrm{Ca}}$ and $c_{\mathrm{Mg}}$. The middle state, $\mathbf{c}_m$, is found where $\mathcal{W}_1$ and $\mathcal{W}_2$ intersect on the hodograph plane. In transport problems, the hodograph plane is commonly referred to as a "composition space" and the waves are described as following the "composition pathways" (Rhee et al., 1989; Lake et al., 2002; Prigiobbe et al., 2012a)

## 3.1 Integral curves and rarefaction waves

The integrated eigenvectors (equation 33) or "integral curves" provide admissible pathways through the composition space in such a way that the conservation laws are not violated (Lax, 1957; Rhee and Amundson, 1972). This is written as,

$$\mathbf{c}_p(\eta) = \mathbf{c}_p(\eta_0) + \int_0^{\eta} \mathbf{r}_p(\eta')d\eta', \tag{35}$$

There are two families of integral curves, one for each conserved solute of the $2 \times 2$ system ($p \in \{1,\ 2\}$). When graphically overlain, these curves form a "net" (Helfferich and Klein, 1970) (Figure 5a). It is at the intersections of the net where possible middle states connected by elementary waves may be found (Prigiobbe et al., 2013b; McNeece and Hesse, 2016a). When an elementary wave connects two constant states with a smooth variation in concentration, these waves are termed $p$-rarefactions, $\mathcal{R}_p$. If the initial composition states $\mathbf{c}_l$ and $\mathbf{c}_r$ are chosen such that they lie along a single integral curve, the $2 \times 2$ system collapses and yields only a single wave. Examples of elementary rarefaction waves for the slow path, $\mathcal{R}_1$, and the fast path, $\mathcal{R}_2$, are shown in the alkaline region of composition space emanating from a single left state in Figure 5a. We present the wave structure using solutions from the alkaline region because the retardation of solute fronts in the acidic region is negligible ($\sigma_p \approx 1$). Thus, the structure of the single elementary rarefaction waves cannot be readily observed in the acidic region.

The continuous solutions for $\mathbf{c}$ are constructed for the native variables $Ca^{2+}$ and $Mg^{2+}$ in Figures 5b-e. The slow and fast path rarefactions are marked $\mathcal{R}_1$ (Figures 5b-c) and $\mathcal{R}_2$ (Figures 5d-e), respectively. The slow path integral curve monotonically decreases in $\theta_1$ while traversing composition space approximately vertically. Along this slow path, calcium and magnesium strongly compete with protons for charged sites on the soil grains and are significantly retarded (Appelo, 1996; Helfferich and Klein, 1970). By inspection, the continuous wave in the constructed solution appears to be a contact discontinuity near $\eta = 0$ (Rhee and Amundson, 1972). In reality, $\mathcal{R}_1$ is a continuous spreading wave with significant retardation. The pseudo-vertical nature of this composition pathway shows that the concentration of magnesium is much more sensitive to adsorption than that of calcium along this path. This is also evident in the constructed solutions for $\mathcal{R}_1$ in $\mathbf{c}$, where magnesium shows a larger compositional change.

The fast path rarefaction, $\mathcal{R}_2$, is significantly less retarded than $\mathcal{R}_1$. In the alkaline region of the composition space, the constructed solutions for $Ca^{2+}$ and $Mg^{2+}$ (Figures 5d-e) demonstrate the continuous spreading behavior typically expected for a rarefaction front (Lax, 1957; Rhee and Amundson, 1972). Along $\mathcal{R}_2$, there is little to no competition between cations and protons for soil adsorption sites. The monotonic decrease in $\theta_2$ is along a composition path where the exchange between $Ca^{2+}$ and $Mg^{2+}$ is nearly 1:1. Because calcium and magnesium share identical valence, substituting one for the other preserves both the total surface charge and the aqueous charge balance simultaneously. The constructed solutions for $Ca^{2+}$ and $Mg^{2+}$ show a nearly congruent absolute change between constant states. The interpretation is that along the fast path, the cations interchange freely to maintain charge balance. Therefore, these are pathways of nearly constant $p$H (Prigiobbe et al., 2013b; McNeece and Hesse, 2016a).

## 3.2 Hugoniot locus and shock waves

The $p$-shock, $\mathcal{S}_p$, is an elementary wave that connects constant end states with a discontinuous jump in composition. The $\mathcal{S}_p$ reaction pathway must conserve mass and charge for the $2 \times 2$ system. These conditions are met by satisfying the Rankine-Hugoniot jump condition (Temple, 1983; Rhee et al., 1989) given as

$$\tilde{\theta}_p(\mathbf{c}^-, \mathbf{c}^+) = \frac{[\mathbf{z}(\mathbf{c})]}{[\mathbf{c}]}. \tag{36}$$

Here, $\mathbf{c}^-$ and $\mathbf{c}^+$ are constant states on the upstream and downstream sides of the shock, respectively. The brackets $[\,\cdot\,]$ denote the jump in the enclosed quantity across the discontinuity. For a given starting state $\mathbf{c}^-$, the Hugoniot locus provides two branches through composition space. These branches, denoted $\mathcal{H}(\mathbf{c}^-)$, are admissible solutions for $\mathbf{c}^+$ that may connect to $\mathbf{c}^-$ with a mass-conserving shock $\mathcal{S}_p$. Moreover, an elementary shock wave $\mathcal{S}_p$ is physically admissible only when the Lax entropy condition (Lax, 1957) is met.

$$\tilde{\theta}_p(\mathbf{c}^-) > \tilde{\theta}_p(\mathbf{c}^-, \mathbf{c}^+) > \tilde{\theta}_p(\mathbf{c}^+), \tag{37}$$

where $p \in \{1, 2\}$. This ensures that the shock is self-sharpening and stable in $\eta$ (Rhee and Amundson, 1972). In this work, the Hugoniot loci dovetail with the integral curves for the continuous solutions, but

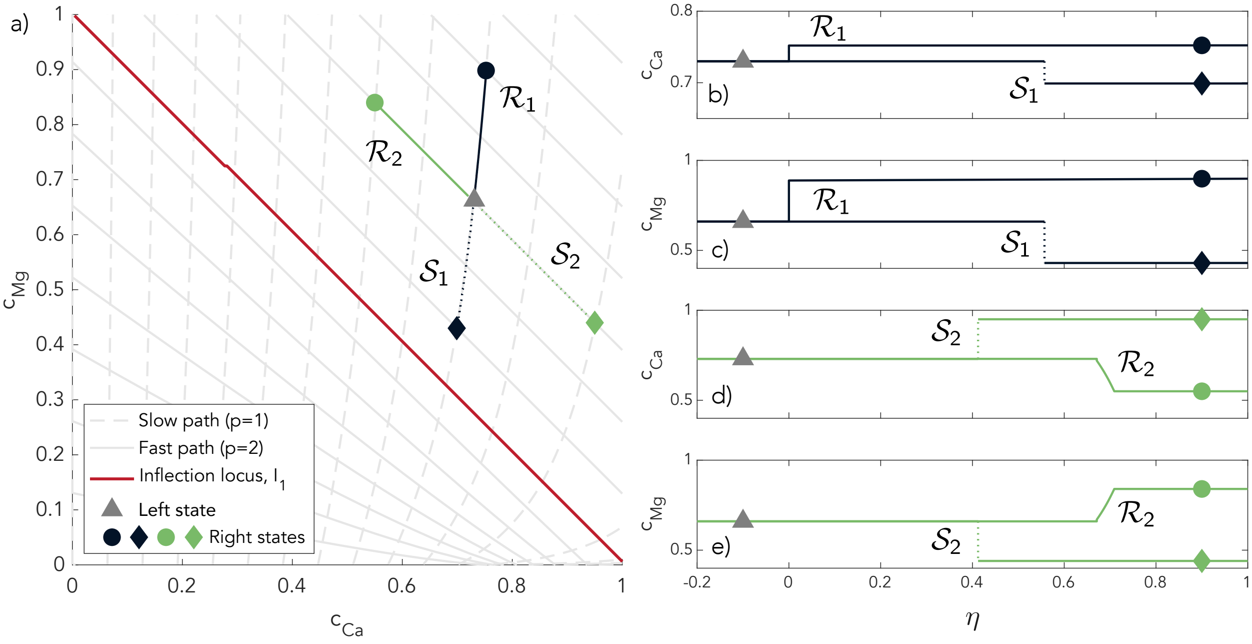

Figure 5: a) Eigenvectors for the characteristic fields $p \in \{1, 2\}$ plotted in composition space. All elementary waves for the Riemann problem can be constructed by following the integral curves along $p = 1$ and $p = 2$ for continuous solutions (i.e. $\mathcal{R}_p$) or against them for discontinuous solutions, $\mathcal{S}_p$. Composite waves arise when $I_1$ is crossed along the first characteristic pathway.

this is not necessary in all cases (Prigiobbe et al., 2013b). Therefore, we henceforth drop the $\mathcal{H}(\mathbf{c}^-)$ notation and simply follow the "net" of the integral curves. In Figure 5, examples of a slow path shock ($\mathcal{S}_1$) and a fast path shock ($\mathcal{S}_2$) are provided along a single branch of the Hugoniot locus at a time. This is analogous to the case where the $p$-rarefactions were plotted along a single $p$ integral curve.

The discontinuous solutions along $\mathcal{S}_1$ and $\mathcal{S}_2$ are constructed for calcium and magnesium in Figures 5b-e. The slow path shock traverses a compositional pathway that dovetails with the integral curves associated with the first characteristic field $\theta_1$. The characteristic pathway is quasi-vertical in composition space in a manner that approximately mirrors $\mathcal{R}_1$ about the $c_{\mathrm{Mg}}$-axis along the same integral curve. Thus, the jump in absolute concentrations of calcium and magnesium is coupled similarly to the $\mathcal{R}_1$ case along this pathway. However, along the compositional pathway for $\mathcal{S}_1$ there is a slight decrease in $\mathrm{Ca}^{2+}$ in the pore water. Counterintuitively, despite the greater magnitude of $\theta_1$ along this pathway, $\mathcal{S}_1$ moves much faster than $\mathcal{R}_1$ when the Rankine-Hugoniot jump condition is satisfied (Equation 36). This is because the compositional pathway for $\mathcal{S}_1$ is moving towards the acidic region of the composition space. In the case of $\mathcal{S}_1$, the soil on the upstream side of the shock is highly acidic, while the soil downstream is relatively less acidic. Therefore, protons increasingly out-compete the divalent cations for charged surface sites, such that calcium and magnesium are unable to adsorb to soil sites. Ultimately, the cations flow more freely with the pore water, and the resultant $\tilde{\theta}_1(\mathbf{c}^-, \mathbf{c}^+)$ only moderately retards the reaction fronts (Figures 5b-c).

The fast path shock $\mathcal{S}_2$, like the fast path rarefaction $\mathcal{R}_2$, lies along a pathway of nearly constant $p$H. These reaction fronts are characterized by the exchange of calcium and magnesium ions at the soil adsorption sites (Prigiobbe et al., 2013b; McNeece and Hesse, 2016a). In the alkaline region (Figure 5a), the increasing calcium concentration in the pore water allows for greater competitive adsorption with magnesium through mass action, despite $K_{\mathrm{Mg}} > K_{\mathrm{Ca}}$ by an order of magnitude. The shock speed $\tilde{\theta}_2(\mathbf{c}^-, \mathbf{c}^+)$ arises because the soil on the upstream side of the shock contains high concentrations of calcium while the soil downstream is relatively depleted in calcium. Therefore, magnesium and undersaturated adsorbed calcium must exchange to balance Equation 36 (Figure 5d-e).

### 3.3 The inflection locus and composite waves

In systems with $p$H-dependent adsorption, characteristic fields may be non-genuinely nonlinear (Liu, 1974). This arises due to the non-convex, competitive Langmuir-type isotherms governing the adsorption of calcium and magnesium. In a case where $\theta_p$ is non-monotonic along a compositional path, elementary waves are not strictly admissible, and a single reaction front takes the form of a composite wave combining a shock and a rarefaction (Ancona and Marson, 2001). This was already observed in earlier works, such as those where reactive transport is controlled by $p$H-dependent adsorption (McNeece and Hesse, 2016a; Prigiobbe et al., 2013b), and in those related to multi-phase flow in porous media (Juanes and Patzek, 2004). The locus of $\max(\theta_p)$ values is defined in composition space as,

$$\nabla\theta_p \cdot \mathbf{r}_p = 0. \tag{38}$$

In the system presented in this manuscript, the fast-path waves ($\mathcal{W}_2$) run perpendicular to the inflection locus in composition space (Prigiobbe et al., 2013b). Only the slow-path waves ($\mathcal{W}_1$) cross $I_1$ and display composite wave behavior. Specifically, the inflection locus can only be crossed when one of the end states lies in the alkaline region and the other in the acidic region. A special type of wave, called a composite wave, arises in the first characteristic field when it joins two composition states $\mathbf{c}$ on opposite sides of the inflection locus, $I_1$. The ordering of the shock and the rarefaction in the composite wave is determined by the shape of the $\theta_1$ function in the neighborhood of the local maximum along $\mathbf{r}_1$ (Liu, 1974; Prigiobbe et al., 2013b). The maximum of $\theta_1$ corresponds to minima in the wave velocity along eigenvector pathways. In this work, shock-rarefaction waves arise for the first characteristic field connecting compositional states that lie on opposite sides of $I_1$. The composite wave $\mathcal{SR}_1$ connects a shock emanating from $\mathbf{c}^-$ to an intermediate point $\mathbf{c}^\star$ on the inflection locus, followed by a rarefaction wave that terminates at $\mathbf{c}^+$. The shock segment $\mathcal{S}_1$ connecting $\mathbf{c}^-$ to $\mathbf{c}^\star$ must satisfy the Liu entropy condition (Liu, 1974) given by

$$\tilde{\theta}_1(\mathbf{c}^-) \geq \tilde{\theta}_1(\mathbf{c}^-, \mathbf{c}^\star) \geq \tilde{\theta}_1(\mathbf{c}^\star), \tag{39}$$

where equality holds at $\mathbf{c}^\star$, ensuring that the shock speed matches the characteristic speed at the junction with the rarefaction. In this manuscript, we have solved for the location of $\mathbf{c}^\star$ where $\mathcal{S}_1$ connects to $\mathcal{R}_1$ quasi-analytically using a combination of analytical solutions and numerical minimization.

#### 3.3.1 Infiltration of alkaline pore water into the acidic region of composition space

In a system where alkaline pore water is injected into the acidic region of composition space, a shock-rarefaction emerges in the first characteristic field ($\mathcal{SR}_1$). To illustrate this, we overlay the first characteristic field, $\theta_1$, and a transect of a single slow path composite reaction front, $A \to A'$ (Figure 6a). Along the transect $A \to A'$, the new intermediate point, $\mathbf{c}^\star$, deviates from the elementary wave behavior shown in Figure 5a. The constructed solutions for calcium and magnesium across the transect show a composite wave wherein a slow-moving shock is combined with a fast-moving rarefaction that satisfies the Liu entropy condition (Equation 39).

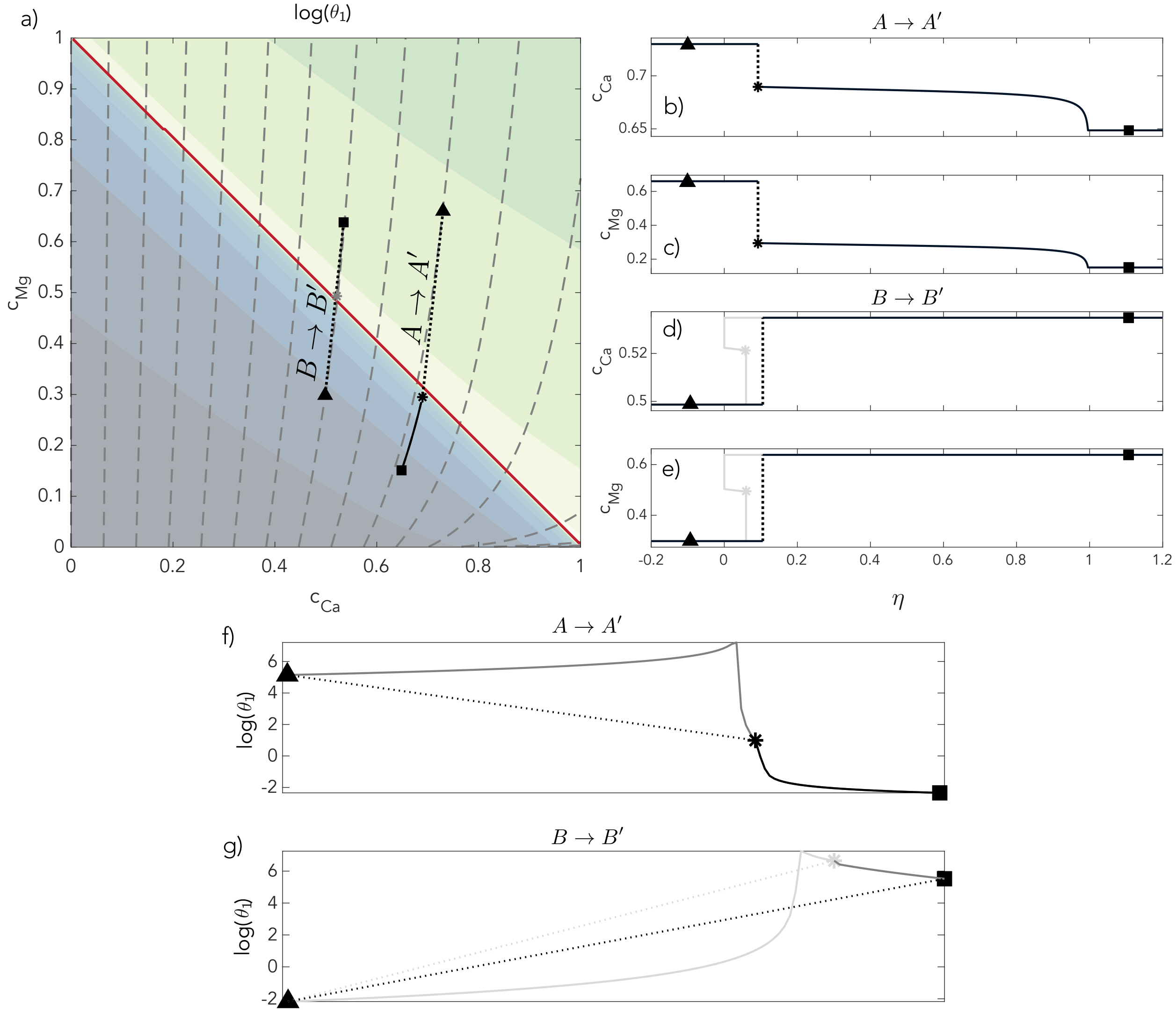

Figure 6: a) The logarithm of the first characteristic field, $\theta_1$, with alkaline-to-acidic ($A \rightarrow A'$) and acidic-to-alkaline ($B \rightarrow B'$) crossing the inflection locus $I_1$. For the case of $A \rightarrow A'$, the tangent point necessitated by the composite wave is plotted between the start, $\triangle$, and end, $\square$, states as a star, $\star$. b) Reconstruction of slow path solution for calcium along $A \rightarrow A'$ showing shock-rarefaction reaction front morphology. For $B \rightarrow B'$, the entropy-condition-violating tangent point is plotted in light gray. c) The corresponding slow path solution reconstruction for magnesium along $A \rightarrow A'$ d) Reconstruction of slow path solution for calcium along $B \rightarrow B'$ exhibiting quasi-elementary shock morphology. e) The corresponding slow path solution reconstruction for magnesium along $B \rightarrow B'$. f) The logarithm of the first characteristic field, $\theta_1$, for the transect $A \rightarrow A'$. The initial and end states bracket the tangent points, resulting in a shock-rarefaction composite wave along the slow pathway through composition space. g) The logarithm of the first characteristic field, $\theta_1$, for the transect $B \rightarrow B'$. In this case, the tangent point is more retarded than the end state (denoted by the gray $\star$ and black $\square$). Thus, the continuous portion of the solution is enveloped by a faster-moving shock and the expressed solution to the Riemann problem along the slow pathway appears to be an elementary shock rather than a composite shock-rarefaction wave.

The shock portion of the composite wave connects $\mathbf{c}_l$ and $\mathbf{c}^\star$ along a shock-path that lies tangent to a new characteristic slow pathway where the rarefaction portion of the wave ensues (Figure 6a-c). As in the case of the elementary waves, the slow paths for the solution to the Riemann problem are characterized by the exchange of cations with protons in the pore water at charged surface sites to maintain charge balance (Appelo, 1996; Helfferich and Klein, 1970). Physically, the shock portion of $A \to A'$ is similar to the elementary wave $\mathcal{S}_1$ in the alkaline region of composition space. The alkaline pore water infiltrates the acidic region causing a shock as calcium and magnesium increase considerably in concentration while protons out-compete the divalent cations for charged surface sites. However, in this case, the terminal state of the shock, $\mathbf{c}^\star$, lies close to $\max(\theta_1)$. In this region of composition space, the competition between the divalent cations and protons for adsorption sites is comparable for all species, and the retardation of calcium and magnesium is moderate, $\tilde{\theta}_{\mathcal{SR}_1}(\mathbf{c}^-, \mathbf{c}^+) \sim 10^0$ (Figure 6f). Constructed solutions for the slow path show that the spreading front of the composite wave that connects $\mathbf{c}^\star$ with $\mathbf{c}_r$ moves at $\eta \approx 1$ (Figures 6b-c). In the rarefaction portion of the composite wave, the mechanism driving the change in cation concentrations of the pore water and reaction front velocity are physicochemically the same as in the shock portion of the wave. The retardation of the back of the rarefaction must match the retardation of the shock for the composite wave to satisfy the entropy condition (Liu, 1974). Once the composite slow wave crosses $I_1$, the remaining portion of $\theta_1$ along the compositional pathway in $A \to A'$ is locally convex and rapidly decreasing. Therefore, the spreading concentration wave spans a region where the retardation due to cation adsorption onto charged surface sites continuously approaches unity ($\sigma_1 \approx 1$) (Figure 6f). In this region of composition space, the pore water solution is acidic enough that the cations are nearly entirely out-competed by protons for adsorption sites on the charged surfaces (for an illustration of the loading isosurface for protons in this region of composition space, see Figure 2c).

### 3.3.2 Infiltration of acidic pore water into the alkaline region of composition space

In a system where acidic pore water is injected into the alkaline region of composition space, an elementary shock $\mathcal{S}_1$ emerges along the slow path rather than a composite shock-rarefaction wave. The shock pathway lies along the characteristic compositional pathway in composition space, as in the case of elementary waves, despite crossing $I_1$ (Figure 6a). The constructed solutions along $B \to B'$ demonstrate the simple moving discontinuity in calcium and magnesium (Figures 6b-c). For the sake of completeness and illustration, we show the tangent point along $B \to B'$, analogous to the case demonstrated in Section 3.3.1 (Figures 6a, d-e, g). In this solution to the Riemann problem along the slow path, the construction of the solution, including a hypothetical intermediate point $\mathbf{c}^\star$, leads to triple-valued solutions, thereby violating the entropy conditions (Figures 6d-e) (Liu, 1974; LeVeque, 2002).

By inspection the difference in $\theta_1$ along the transects $A \to A'$ and $B \to B'$ are readily apparent. In the case of $A \to A'$, the retardation of the composed wave decreases monotonically because the intermediate point, $\mathbf{c}^\star$ and the resultant shock remain more retarded than the continuous portion of the wave (Figure 6f). Along the transect $B \to B'$, however, the shock formed while crossing $I_1$ results in a rarefaction that is more retarded than the shock formed by the left state and the right state along the characteristic pathway (Figure 6g). In essence, the solution to the Riemann problem yields a composite wave containing a rarefaction, which is immediately enveloped by a faster moving shock (Figures 6d-e).

The compositional morphology of the reaction front along $B \to B'$ occurs due to the protonation of the adsorption sites on the soil along the reaction front. As the acidic water enters the alkaline region, the acidity liberates cations from adsorption sites causing a positive jump in both calcium and magnesium (Figures 6d-e). Because $K_{\mathrm{H}} \gg K_{\mathrm{Ca,Mg}}$, and the upstream surplus of protons infiltrating

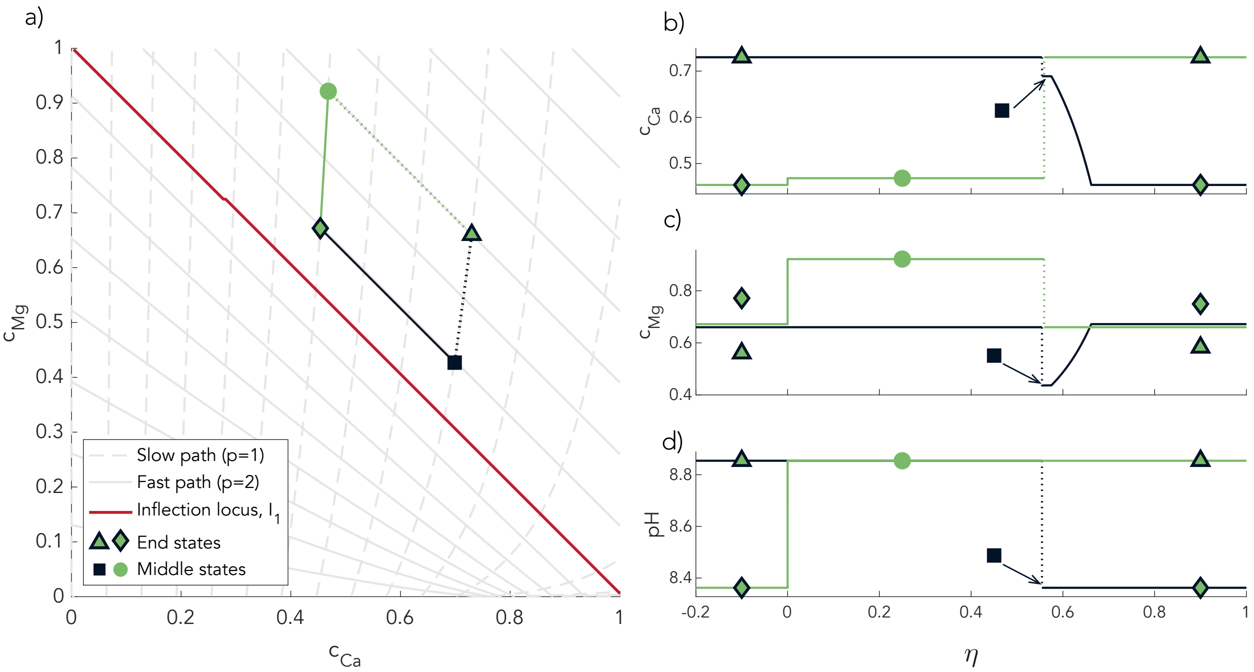

Figure 7: a) The solution net of slow and fast characteristic pathways plotted through the alkaline region of composition space. The so-called "end states" can be either left or right states. When △ is the left state, the lower branch of the solution to the Riemann problem ensues and ☐ marks the middle-state, $\mathbf{c}_m$. The lower branch of the solution in alkalinity space connects the end states with the structure $\mathbf{c}_l \xrightarrow{\mathcal{S}_1} \mathbf{c}_m \xrightarrow{\mathcal{R}_2} \mathbf{c}_r$. When ◊ marks the left state, the upper branch of the solution is required, and ◯ marks the middle state. The resultant structure is $\mathbf{c}_l \xrightarrow{\mathcal{R}_1} \mathbf{c}_m \xrightarrow{\mathcal{S}_2} \mathbf{c}_r$. b) The reconstructed solution for $c_{\mathrm{Ca}}$ for both branches of the solution to the Riemann problem. c) The reconstructed solution for $c_{\mathrm{Mg}}$ for both branches of the solution to the Riemann problem. d) The reconstructed solution for $p$H for both branches of the solution to the Riemann problem.

from the acidic region, the soil cannot adsorb the incoming acidity faster than the protons are supplied thereby forming an elementary shock, $\mathcal{S}_1$.

### 3.4 The full structure of solutions to the Riemann problem

In the previous sections of the manuscript, we presented solutions to the Riemann problem that explicitly lie along a single slow- or fast-characteristic pathway through composition space. For clarity of presentation, we isolated the fundamental structures possible for $\mathcal{W}_1$ and $\mathcal{W}_2$ separately. We now construct the full solutions for the $2 \times 2$ system of conservation laws for which we are solving the Riemann problem. The left compositional state, $\mathbf{c}_l$, is connected to the right state, $\mathbf{c}_r$, by a middle state, $\mathbf{c}_m$ (Lax, 1957; Rhee and Amundson, 1972) (see equation 34). Given the possible combinations of $\mathbf{c}_l$ and $\mathbf{c}_r$ and their relative positions in composition space, there are eight fundamental structures of the solutions to the Riemann problem (Prigiobbe et al., 2013b).

### 3.4.1 Solutions for the Riemann problem in the acidic region of composition space

The acidic region of composition space yields solutions to the Riemann problem constructed by elementary waves. In this region, the adsorption of protons dominates charged surface sites on the soil grains. Thus, for both the slow- and fast-path waves, the retardation is negligible ($\sigma_p \approx 1$, $\theta_p \approx 0$). In other words, the wave structure of the Riemann problem persists mathematically, but there is nearly no lag of $c_{\mathrm{Ca}}$ or $c_{\mathrm{Mg}}$ compared to the bulk velocity of the aqueous solution, rendering the reactive fronts observationally indistinguishable from passive transport. Changes in the pore water $p$H due to the adsorption and desorption of cations are minuscule, as protons entirely out-compete the divalent cations for all charged surface sites (Prigiobbe et al., 2013b; McNeece and Hesse, 2016a). Therefore, in highly acidified soil, where the strong ion difference is positive (i.e. acid mine drainage conditions or similar experimental conditions), there will be little to no discernible lag of charged solutes due to adsorption during transport (Blowes et al., 1994; Jurjovec et al., 2002).

### 3.4.2 Solutions to the Riemann problem in the alkaline region of composition space

In the case where both the left and right states plot above the inflection locus $I_1$ in composition space, solutions to the Riemann problem are constructed from elementary waves shown in Figure 5. Unlike the case in the acidic region, the divalent cation solute fronts experience significant retardation due to adsorption onto charged surface sites (Appelo, 1996; Helfferich and Klein, 1970). Here, the morphology of the constructed solution is highly dependent on the orientation of the end states with respect to one another (Figure 7). Principally, $K_{\mathrm{Mg}} > K_{\mathrm{Ca}}$ dictates the primary shape of the solute front morphology across $\mathcal{W}_1$ and $\mathcal{W}_2$ (Rahnemaie et al., 2006a). The slow path reaction, $\mathcal{W}_1$, is characterized by large changes in $c_{\mathrm{Mg}}$ coupled with relatively small changes in $c_{\mathrm{Ca}}$. More generally, in this region of composition space, there are two branches of the solution. Here we distinguish the solutions by designating the nomenclature "upper branch" and "lower branch" solutions based on the pathway orientation through the composition space. The upper branch solution has an initial state where the calcium concentration is low relative to the end state. Solutions of this type require an intermediate increase in $c_{\mathrm{Mg}}$ along the slow path ($\Diamond \xrightarrow{\mathcal{R}_1} \bigcirc$ Figure 7). By inspection of Figure 4a, it is apparent that the solute front will be highly retarded compared to the bulk pore water velocity $\bar{v}$ in the alkaline region of composition space for the first characteristic field $\theta_1$. For the solution case presented here, the value of $\theta_1$ ranges from $\sim 10^6$ to $10^4$. Thus, the continuous solution has the effective appearance of a contact discontinuity with $v_1 \approx 0$ relative to the bulk pore water velocity. The fast path, which connects the middle and end states for the upper branch solution, is a shock; $\mathcal{S}_2$ ($\bigcirc \xrightarrow{\mathcal{S}_2} \triangle$ in Figure 7). This elementary shock $\mathcal{S}_2$ is only moderately retarded ($\theta_2 \sim 10^{-1}$) compared to the bulk pore water velocity (Figures 7b-d). The lower branch of the solution occurs when the initial state is high in calcium relative to the end state. In such a case, the full solution to the Riemann problem is constructed by a shock along the slow path and a subsequent rarefaction following the integral curves for the fast path. Crucially, the behavior associated with the adsorption and exchange of magnesium is inverted compared to the upper branch of the solution on the slow path; $\mathcal{S}_1$ ($\triangle \xrightarrow{\mathcal{S}_1} \square$ in Figure 7). Another crucial feature of $\mathcal{S}_1$ for the lower branch of the solution in the alkaline region of composition space is that the retardation of the solute front relative to the pore water is moderate; $\tilde{\theta}_1 \sim 10^{-1}$. Therefore, the shock that forms moves at a velocity comparable to that of the bulk pore water velocity, albeit measurably retarded. The fast path portion of the solution is continuous and follows the integral curves for the second characteristic field; $\mathcal{R}_2$ ($\square \xrightarrow{\mathcal{R}_2} \Diamond$ in Figure 7). For the example presented here, this elementary rarefaction connecting

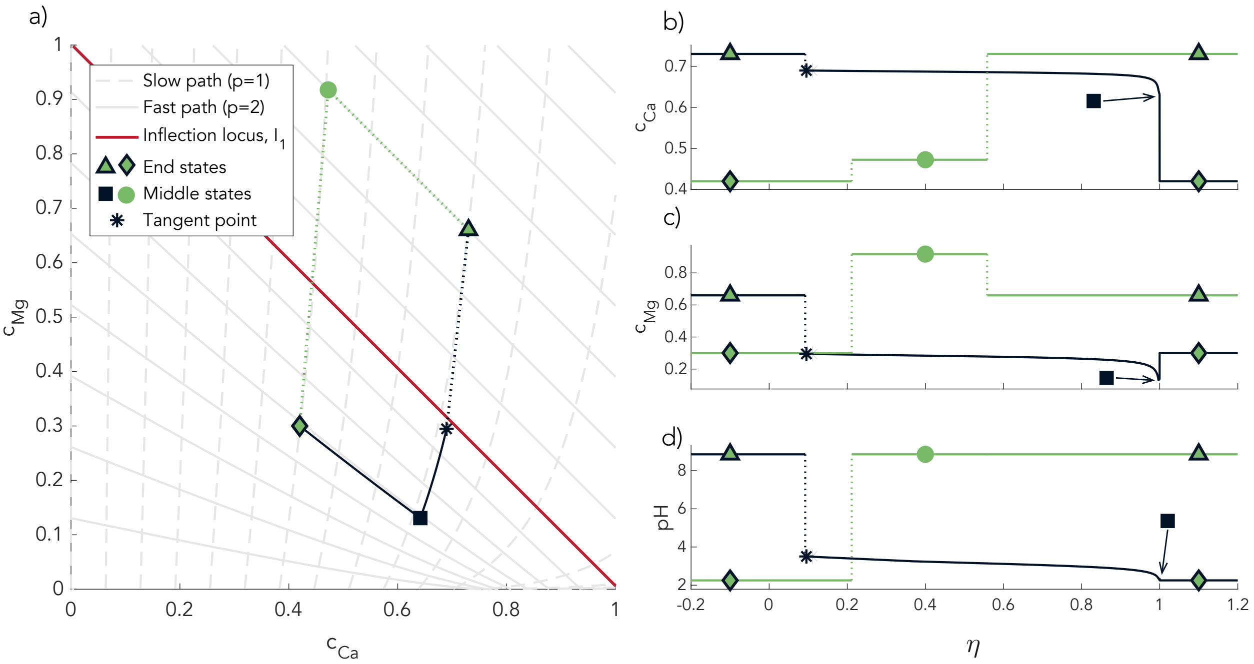

Figure 8: a) The solution net of slow and fast characteristic pathways plotted through the alkaline region of composition space. The convention for left and right states as they correspond to end states and solution branches is the same as in Figure 7. Here, the slow path of the lower branch of the solution is a composite wave such that the construction of the solution takes the form, $\mathbf{c}_l \xrightarrow{\mathcal{S}_1} \mathbf{c}_i \xrightarrow{\mathcal{R}_1} \mathbf{c}_m \xrightarrow{\mathcal{R}_2} \mathbf{c}_r$, where the subscript $i$ denotes an "intermediate" state along the slow path. For the majority of this manuscript we collapse this notation to the shorthand $\mathbf{c}_l \xrightarrow{\mathcal{SR}_1} \mathbf{c}_m \xrightarrow{\mathcal{R}_2} \mathbf{c}_r$, to emphasize the composite nature of the solute front on the slow path. The upper branch of the solution does not require a composite wave despite crossing $I_1$. In the case of the upper branch $\mathbf{c}_l \xrightarrow{\mathcal{S}_1} \mathbf{c}_m \xrightarrow{\mathcal{S}_2} \mathbf{c}_r$. b) The constructed solutions for $c_{\mathrm{Ca}}$ for both branches of the solution to the Riemann problem. c) The constructed solutions for $c_{\mathrm{Mg}}$ for both branches of the solution to the Riemann problem. d) The constructed solutions for $p\mathrm{H}$ for both branches of the solution to the Riemann problem.

the middle state to the right end state is only moderately less retarded than the slower moving shock (Figures 7b-d).

### 3.4.3 Inter-regional solutions for the Riemann problem in composition space

We now explore solutions to the Riemann problem where the end states of the solution plot on either side of $I_1$ in composition space. As in the cases discussed in Section 3.4.2, for any given pair of end states, there are two possible branches of the solution. For the composition space construction presented here we chose the same nomenclature for the "upper" and "lower" branches. The upper branch is characterized by an increase in $c_{\mathrm{Mg}}$ between the end states whereas the lower branch has an intermediate decrease. Along the upper branch of the solution, the slow path is a shock, $\mathcal{S}_1$ ($\Diamond \xrightarrow{\mathcal{S}_1} \bigcirc$ in Figure 8). This solute reaction front morphology arises due to the dynamics discussed in Section 3.3.1 along the pathway $B \to B'$ (Figures 6a, g) (Liu, 1974). After the shock from the acidic region into the alkaline region, the fast path ensues as an elementary shock, $\mathcal{S}_2$, moving along the integral curves $(\bigcirc \xrightarrow{\mathcal{S}_2} \triangle)$. In this case, $\mathcal{S}_2$ lies within the alkaline region of composition space and is moderately retarded compared to the bulk velocity of the pore water. For the lower branch of the solution, the slow path is a composite shock-rarefaction wave, $\mathcal{SR}_1$, akin to the reaction front described in Section 3.3.1 along $A \to A'$. The value of $\theta_1$ decreases rapidly when moving across the inflection locus $I_1$ from the alkaline region of composition space to the acidic region. The rarefying portion of $\mathcal{W}_1$ $((*) \xrightarrow{(*)\mathcal{R}_1} \square)$ connects a shock of moderate retardation with a front moving with virtually no retardation ($\sigma_1 \approx 1$, $\theta_1 \approx 0$). As discussed previously, the acidic region of composition space has virtually no available adsorption sites for calcium or magnesium because charged surface sites are monopolized by protons. Thus, the continuous solution connecting the middle state with the end state effectively moves at the bulk fluid velocity $(\square \xrightarrow{\mathcal{R}_2} \Diamond)$.

# 4 Discussion

## 4.1 Compound waves and the sigmoidal proton isotherm

A central result of this work is that the sigmoidal nature of proton adsorption onto charged mineral surfaces fundamentally alters the structure of reactive transport in soils. Because the proton adsorption isotherm is both strongly nonlinear and dominant at low *p*H ($K_{\mathrm{H}} \gg K_{\mathrm{Ca}}, K_{\mathrm{Mg}}$), the resulting loading isosurfaces are non-convex in composition space. This non-convexity gives rise to non-genuinely nonlinear characteristic fields and, consequently, to composite shock–rarefaction waves in the slow characteristic family (Liu, 1974).

Physically, these composite waves reflect a transition in the dominant charge-balancing mechanism along the reaction front. In alkaline pore waters, divalent cations compete effectively for charged surface sites, leading to significant retardation of solute fronts. As the reaction front migrates into acidic regions, proton adsorption rapidly saturates the surface sites, suppressing cation adsorption and collapsing retardation toward unity. The resulting mismatch in wave speeds across the inflection locus produces a composite reaction front: a slow shock followed by a faster rarefaction. This mechanism is generic to systems where acidity strongly controls surface complexation and is not specific to the particular parameter choices explored here.

The practical consequence is that *p*H-dependent adsorption introduces a qualitative asymmetry in how alkalinity fronts propagate through soils. Fronts moving from alkaline into acidic pore water encounter a region where retardation drops sharply, producing a self-sharpening shock at the leading edge followed by a dispersive tail (Rhee and Amundson, 1972; Helfferich and Klein, 1970). This asymmetry has direct implications for how alkalinity generated by enhanced rock weathering is retained, redistributed, and ultimately exported from the soil profile.

## 4.2 The role of the Péclet number

The analysis presented here focuses on the advection-dominated limit ($\mathrm{Pe} \gg 1$), which isolates the role of nonlinear adsorption in shaping reaction front structure. In field settings, dispersion and diffusion may partially smear sharp fronts, particularly in heterogeneous soils or under low flow velocities. Finite Péclet numbers will regularize shocks into thin transition zones and broaden rarefactions, but will not eliminate the underlying wave hierarchy or the dependence of retardation on *p*H-controlled adsorption (LeVeque, 2002; Rhee et al., 1989).

Many agricultural and managed landscapes targeted for enhanced rock weathering experience episodic infiltration events. For example, monsoon rains and irrigation pulses naturally come with with high local Péclet numbers. During such events, the advection-dominated assumption is appropriate. Here, soil columns may behave transiently as chromatographic systems, selectively retaining or releasing alkalinity depending on the evolving chemical state of the pore water (Helfferich and Klein, 1970; Appelo, 1996). Between infiltration events, diffusion-dominated conditions may allow partial re-equilibration of exchange sites with ambient pore water, effectively resetting the initial conditions for the next advective pulse. The interplay between episodic advection and inter-event diffusion could produce complex, pulsatile alkalinity export signatures that defy interpretation by steady-state models. While a full treatment of this coupling is beyond the scope of the present work, the wave structures identified here provide the necessary building blocks for constructing such models (Smoller, 1994; Dafermos, 2005), the Riemann solutions define the asymptotic behavior toward which each advective pulse evolves (Rhee et al., 1989; Helfferich and Klein, 1970), and the characteristic speeds determine how rapidly fronts separate under field flow conditions (Temple, 1983; LeVeque, 2002).

## 4.3 Role of the strong ion difference

In this analysis, background anions enter the governing equations through the strong ion difference, $c_a$ (equation 20). While $c_a$ is treated as a conservative quantity, it exerts a first-order control on the position of the inflection locus $I_1$ and therefore on the topology of the integral-curve net in composition space (Figure 9).

The physical significance of $c_a$ becomes very clear when it is connected to the conceptual framework introduced by Hamilton et al. (2007) for agricultural liming. Whether silicate dissolution sequesters atmospheric $CO_2$ depends on whether weathering is driven by carbonic acid, producing bicarbonate alkalinity, or by strong acids such as $HNO_3$ and $H_2SO_4$, which charge-balance the released cations without generating durable carbon storage (Hamilton et al., 2007; Hartmann et al., 2013). In the notation of the present model, this distinction maps directly onto $c_a$: large positive values of $c_a$ indicate a pore water dominated by strong acid anions (e.g., from ammonium-based fertilizers or acid deposition), whereas small or negative values correspond to systems where carbonic acid is the principal weathering agent. In acidic tropical soils where strong acids accounted for over 98% of measured basalt dissolution, in-field $CO_2$ removal was negligible despite substantial mineral weathering (Holden et al., 2024). However, not all acidic tropical soils are strong-acid dominated. In warm, biologically productive systems, root and microbial respiration can elevate soil $pCO_2$ to $10^{-1.5}$–$10^{-1}$ atmospheres, (Amundson et al., 1998; Cerling, 1984), making carbonic acid the principal weathering agent even at low $p$H (Perez-Fodich and Derry, 2019). Whether a given acidic soil falls in the strong-acid or carbonic-acid regime cannot be inferred from $p$H alone. It requires characterization of the ratio of base cations to bicarbonate alkalinity.

To illustrate this effect, we construct integral-curve nets for two reference states that share identical divalent cation concentrations but differ only in the sign of $c_a$ (Table 2). The acidic state ($c_a = +6 \times 10^{-3}$ mol L$^{-1}$, $p\text{H} \approx 2.7$) represents pore water in which strong acid anions dominate the charge balance, while the alkaline state ($c_a = -6 \times 10^{-3}$ mol L$^{-1}$, $p\text{H} \approx 7.5$) represents a system where carbonic acid is the principal weathering agent. Figure 9a illustrates the theoretical 1:1 equivalence between base cations ($Ca^{2+} + Mg^{2+}$) and bicarbonate alkalinity expected under pure carbonic acid weathering (Hamilton et al., 2007). States above this line (blue region) indicate an excess of cations over alkalinity, implying that strong acids have contributed to dissolution without corresponding $CO_2$ sequestration. States below the line (green region) indicate efficient carbon drawdown. Figures 9b-c show how the integral-curve net in composition space differs between these two regimes. The composition-space

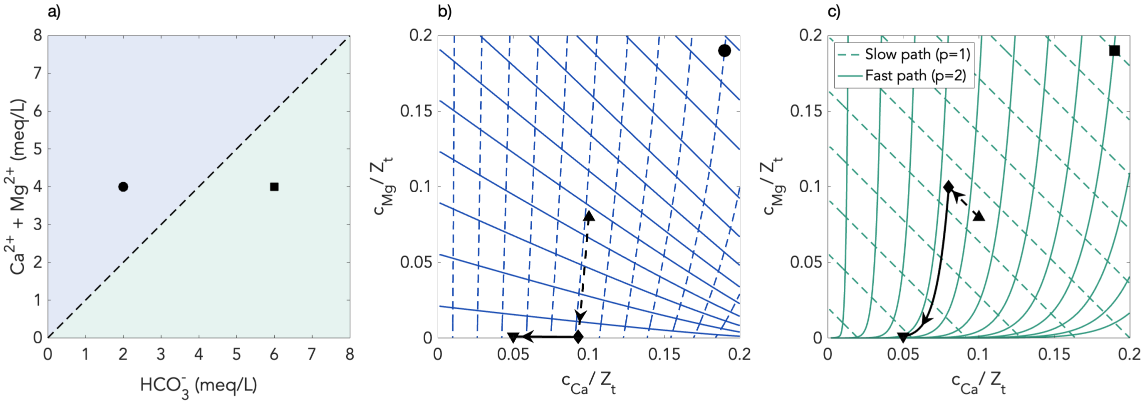

Figure 9: a) “Hamilton plot” showing theory for acidity sources in weathering. In the blue region, above the dotted line, silicate weathering is inefficient due to acid contributions that cannot be accounted for by the carbonic acid system. The dotted line represents the theoretical case where acidity from the carbonic acid system is balanced by alkalinity generated by basalt rock feedstock dissolution. In the green region, below the dotted line, alkalinity generation from rock weathering favors efficient carbon dioxide drawdown. b) The integrated slow- and fast pathways through composition space that correspond to the state marked by the point in the blue region above the dotted line. c) The integrated slow- and fast pathways through composition space that correspond to the state marked by the black square beneath the dotted line in the Hamilton plot. In panels b) and c), the left and right end states are the same reference composition, and $\Diamond$ marks the intermediate state. The pathways shown are illustrative; in an experiment or natural system, the observed breakthrough curve would correspond to a shift from the right state, $\bigtriangledown$, toward the intermediate state, $\Diamond$.

topology, therefore the accessible wave structures, changes qualitatively as $c_a$ varies. Identical Ca$^{2+}$–Mg$^{2+}$ end states can produce fundamentally different transport behavior depending on background ionic composition. This is because the topology of the integral-curve nets predicts differential fractionation of Ca$^{2+}$ and Mg$^{2+}$ during breakthrough. Early-time Ca/Mg ratios in drainage waters thus provide a diagnostic for the retardation regime. By extension, Ca/Mg ratios indicate if the system is operating in the carbonic-acid or strong-acid weathering domain without requiring direct measurement of $c_a$ itself, so long as the initial state of the system (right state) has been characterized.

Because the cation wave speeds and retardation factors depend on $c_a$, two sites with identical feedstock application rates and similar soil $p$H can produce markedly different cation breakthrough signatures depending on whether the acidity is carbonic or strong-acid in origin. At a high-$c_a$ site, low retardation means that weathering-derived cations pass through the profile rapidly and appear in drainage on short timescales. If charge-balanced by nitrate or sulfate rather than bicarbonate, a large cation flux may be accompanied by only modest changes in alkalinity. At a low-$c_a$ site with comparable $p$H but high $p\mathrm{CO}_2$, the same cations are significantly retarded by exchange onto charged surface sites, producing an extended delay before cation breakthrough while bicarbonate moves ahead relatively unimpeded. The observational consequence is a persistent deficit of cations relative to alkalinity in drainage. This is a potential mechanism for explaining “missing alkalinity” signature observed in ERW experiments (Kelland et al., 2020; Hasemer et al., 2024; te Pas et al., 2024). This is a predictable consequence of chromatographic retardation rather than evidence for permanent cation sinks such as the formation of

Table 2: Parameters and reference states for the strong ion difference comparison (Figure 9). Both states share the global parameters listed below; only $c_a$ differs.

| **Parameter** | **Symbol** | **Value** |
|---|---|---|
| *Global chemical and transport parameters* | | |
| Total surface site concentration | $Z_t$ | $10^{-2}$ mol $L^{-1}$ |
| Porosity ratio | $\varphi$ | 4 |
| Partial pressure of $CO_2$ | $pCO_2$ | $10^{-2}$ atm |
| Henry's constant | $h_c$ | 29 (L·atm)/mol |
| $Ca^{2+}$ adsorption constant | $K_{Ca}$ | $10^3$ L/mol |
| $Mg^{2+}$ adsorption constant | $K_{Mg}$ | $10^4$ L/mol |
| $H^+$ adsorption constant | $K_H$ | $10^8$ L/mol |
| First dissociation constant of carbonic acid | $K_1$ | $10^{-6}$ mol/L |
| Water dissociation constant | $K_w$ | $10^{-14}$ $(mol/L)^2$ |
| *Reference states* | | |
| | **Acidic state** | **Alkaline state** |
| $c_{Ca}$ (mol $L^{-1}$) | $1.0 \times 10^{-3}$ | $1.0 \times 10^{-3}$ |
| $c_{Mg}$ (mol $L^{-1}$) | $1.0 \times 10^{-3}$ | $1.0 \times 10^{-3}$ |
| $c_a$ (mol $L^{-1}$) | $+6.0 \times 10^{-3}$ | $-6.0 \times 10^{-3}$ |
| $c_H$ (mol $L^{-1}$) | $2.0 \times 10^{-3}$ | $3.4 \times 10^{-8}$ |
| $p$H | 2.70 | 7.46 |

secondary silicate minerals.

## 4.4 Chromatographic retardation and the "missing alkalinity"

A recurring observation across ERW field trials is that base cation release substantially exceeds the bicarbonate or dissolved inorganic carbon (DIC) flux measured in soil pore water or drainage (Kelland et al., 2020; Hasemer et al., 2024; te Pas et al., 2024; Hammes et al., 2025). This discrepancy is variously attributed to secondary mineral formation (authigenic clays, amorphous silica, metal oxyhydroxides), plant uptake, or soil carbonate precipitation (Clarkson et al., 2024; Hartmann et al., 2013). While each of these sinks undoubtedly operates to some degree, the chromatographic framework developed here identifies a complementary mechanism for explaining the apparent alkalinity deficit.

The retardation factors derived here show that divalent cation fronts in circumneutral to alkaline pore waters can be retarded by factors of 5–50 or more relative to the advective velocity, depending on CEC and the position in composition space. The mechanism by which this delays alkalinity export is straightforward. When weathering-derived $Ca^{2+}$ or $Mg^{2+}$ adsorbs onto a charged surface site, it displaces the ion previously occupying that site. In the case of acidic to circumneutral soils, predominantly $H^+$. The displaced protons re-enter the pore water and titrate the bicarbonate that accompanied the divalent cations, converting $HCO_3^-$ back to carbonic acid. The cation deficit on the aqueous side is matched by the loss of bicarbonate alkalinity. The net effect is that both cations and alkalinity are consumed in the exchange zone, with cations partitioning onto the solid phase, bicarbonate reverting to carbonic acid. Drainage water downstream of the exchange front is therefore depleted in both base cations and alkalinity relative to what the dissolution rate alone would predict. During the transient period before the exchange front breaks through, cation adsorption temporarily reverses the CDR reactions by regenerating $CO_2$ from bicarbonate (Appelo, 1996; Clarkson et al., 2024). It is worth noting here, that this is not equivalent to re-emission (Kelland et al., 2020; Hasemer et al., 2024; te Pas et al., 2024; Hammes et al., 2025).

Unlike cations locked into secondary clay minerals, exchangeable cations will desorb and export as the exchange front migrates deeper into the profile. The wave structures derived here predict the timing and shape of this delayed export. The breakthrough curve should exhibit a characteristic lag. Recent work has begun to recognize this distinction. te Pas et al. (2024) introduced the concept of a "retarded fraction" of weathering products retained within the soil profile and showed that soil-based mass balance estimates of CDR converge with leachate-based alkalinity measurements only after correcting for this fraction. However, the reservoir containing the "missing" cations remained elusive to the workers. Recently, Kanzaki et al. (2024) modeled cation storage on exchange sites and found that desorption timescales can range from years to decades depending on soil properties and hydrological regime. The present work provides a simple theoretical framework for explaining these observations by explicitly resolving how *p*H-dependent retardation partitions alkalinity between mobile and immobile phases.

The distinction has direct consequences for long term carbon accounting. Cations retained on exchange sites represent delayed CDR. Cations incorporated into authigenic clays or oxyhydroxides may represent a longer-term or permanent sink that does not generate bicarbonate export (Clarkson et al., 2024; Hammes et al., 2025). Conflating the two mechanisms risks either overestimating CDR, if exchangeable cations are counted as permanent removal, or underestimating it, if the eventual export of retarded cations is ignored. The wave structures identified here provide testable predictions for distinguishing these mechanisms: retardation should produce characteristic temporal signatures in breakthrough curves, delayed onset followed by predictable front shapes, that differ qualitatively from the monotonic depletion expected if cations are consumed by irreversible mineral precipitation.

## 4.5 Non-uniqueness in MRV and the role of mechanistic models

A recurring challenge in enhanced rock weathering monitoring, reporting, and verification (MRV) is the non-uniqueness of observable signals. Similar downstream alkalinity or DIC fluxes may arise from fundamentally different subsurface processes-transient storage on exchange sites, delayed release following front propagation, direct export, or cation loss to secondary minerals (Clarkson et al., 2024; Hammes et al., 2025). Cation-based and carbon-based MRV approaches can yield divergent CDR estimates precisely because they are sensitive to different components of this partitioning (Hasemer et al., 2024; te Pas et al., 2024).

The theoretical framework developed here helps reduce this ambiguity by linking observable transport behavior to underlying adsorption dynamics and wave structures. By explicitly resolving how *p*H-dependent surface reactions partition weathering products between mobile and immobile phases, the model provides a mechanistic basis for predicting which fraction of released cations will appear as bicarbonate-balanced alkalinity in drainage and on what timescale. While the model is simplified-it neglects dissolution kinetics, secondary mineral precipitation, biological uptake, and soil heterogeneity, it provides first-order controls on cation retardation and front structure that must be understood before these additional complexities can be meaningfully interpreted.

We note that the method of characteristics solutions developed here, while analytically derived for idealized boundary conditions, could serve as back-of-the-envelope estimates for alkalinity budgets at larger scales. The characteristic speeds and retardation factors provide order-of-magnitude predictions of cation residence times in the soil column, which could be compared against observed export timescales to assess whether retardation alone is sufficient to explain the apparent cation deficit, or whether additional sinks must be invoked. Such estimates would complement the increasingly sophisticated reactive transport simulations being developed for ERW systems (Kanzaki et al., 2024) by providing transparent, physically grounded benchmarks against which numerical models can be validated.

## 4.6 Experimental design and site selection for ERW

The results presented here motivate a mechanistic framing of how ERW experiments and deployments are designed and interpreted.

### 4.6.1 Soils as chromatographic media.

Column experiments that impose controlled alkaline-to-acidic transitions rather than steady-state boundary conditions would be particularly valuable for testing the compound wave behavior predicted by this analysis. Step-change or pulse-input experiments, in which an alkaline influent (simulating rock weathering products) displaces acidic pore water, should produce the composite shock–rarefaction structures derived here. Measuring both cation and alkalinity breakthrough curves at multiple depths would allow direct comparison with the predicted wave speeds and front shapes. Critically, such experiments must extend well beyond the expected cation arrival time. If chromatographic retardation is the dominant mechanism, the "missing" cations should eventually appear downstream with a characteristic front shape that matches the predicted wave structure. If secondary mineralization dominates instead, the cation deficit should persist or grow with time. At larger field scales, lysimeter or small-watershed studies could investigate whether the delayed, pulsatile alkalinity export predicted by the retardation analysis emerges following ERW deployment.

Isotopic tracers in leachate offer a complementary diagnostic for resolving retardation from secondary mineral formation. Lithium isotopes ($\delta^7$Li) are particularly well suited because $^6$Li is preferentially incorporated into neoformed clays during incongruent weathering, driving residual dissolved $\delta^7$Li to heavier values than the forming solid (Pistiner and Henderson, 2003; Pogge von Strandmann et al., 2020; Hindshaw et al., 2019). Reversible cation exchange on pre-existing surfaces produces comparatively negligible fractionation If the cation deficit in the pore water breakthrough is dominated by chromatographic retardation, dissolved $\delta^7$Li should remain close to the feedstock value if weathering is roughly congruent and the "missing" cations are held reversibly on exchange sites rather than locked into new mineral phases. If authigenic clay formation is significant, leachate $\delta^7$Li should be elevated well above feedstock values, reflecting the preferential removal of $^6$Li into secondary silicates (Dellinger et al., 2015; Pogge von Strandmann et al., 2017). Similarly, $\delta^{26}$Mg fractionates strongly during clay precipitation but negligibly during exchange (Tipper et al., 2006; Clarkson et al., 2024), and $\delta^{30}$Si can distinguish amorphous silica precipitation from congruent dissolution (Ziegler et al., 2005). Column or field experiments that pair time-resolved cation and alkalinity breakthrough curves with $\delta^7$Li measurements in leachate would provide a direct, first-order test where elevated $\delta^7$Li would implicate irreversible clay formation as the dominant sink.

### 4.6.2 Site selection and strong ion difference $c_a$

The connection between strong ion difference $c_a$ and CDR efficiency (Figure 9a) provides a practical screening tool for ERW deployment. Sites with low strong acid loads-low nitrogen fertilizer input, minimal acid deposition, circumneutral background $p$H-will sit closer to or below the 1:1 line, where carbonic acid weathering dominates and CDR per unit dissolution is maximized (Hamilton et al., 2007). Sites with high $c_a$ (heavily fertilized, acid sulfate soils, AMD-impacted) may still benefit agronomically from $p$H correction, but will deliver less carbon removal per tonne of feedstock applied and will exhibit less retardation of weathering products in the soil profile. Measuring $c_a$-or equivalently, characterizing the strong acid anion budget (nitrate, sulfate, chloride) relative to sodium-before deployment would help predict both CDR efficiency and the expected timescale for alkalinity export. These recommendations are not novel. However, using early-time Ca/Mg ratios in drainage waters as diagnostic for the carbonic-acid or strong-acid weathering domain is a new suggestion (see Figure 9b-c).

# 5 Conclusions

We have shown that the nonlinear, $p$H-dependent adsorption of protons and divalent cations onto charged mineral surfaces gives rise to compound shock–rarefaction waves in the reactive transport of alkalinity through soils. The sigmoidal proton isotherm produces non-convex loading isosurfaces and, consequently, non-genuinely nonlinear characteristic fields whose structure is strongly controlled by the strong ion difference, $c_a$. This parameter maps directly onto the distinction between carbonic-acid and strong-acid weathering regimes, linking the mathematical structure of the conservation laws to a quantity of immediate practical relevance for the site dependent efficiency of CDR.

Divalent cation fronts in circumneutral to alkaline pore waters are moderately retarded relative to the advective velocity of pore water. Because cation adsorption displaces protons that titrate the accompanying bicarbonate, both cations and alkalinity are consumed together in the exchange zone, temporarily reversing the CDR reaction until the exchange front breaks through. This mechanism accounts for much of the "missing alkalinity" observed in field trials without invoking permanent mineral sinks. We find that the differential selectivity $K_{\mathrm{Mg}} > K_{\mathrm{Ca}}$ causes early breakthrough to be enriched in $\mathrm{Ca}^{2+}$ relative to feedstock stoichiometry when pore water $p$H is sufficiently high that cation retardation is significant. At lower $p$H, the breakthrough is dominated by calcium as protons monopolize charged surface sites (Figure 9b). The timing of these fronts is governed by the eigenvalues $\theta_1$ and $\theta_2$ (Figure 4), which vary by orders of magnitude between the alkaline and acidic regions of composition space. These contrasting breakthrough signatures make early-time Ca/Mg ratios a potential diagnostic for identifying the active weathering regime, provided the initial pore water composition has been sufficiently characterized. Lastly, the characteristic speeds and wave structures provide transparent, back-of-the-envelope benchmarks for cation residence times against which numerical reactive transport models and field observations can be compared.

# Acknowledgments

J.S.J. is employed by Mati Carbon PBC. M.A.S. acknowledges the financial support received through the Future Faculty in the Physical Sciences Postdoctoral Fellowship from Princeton University. N.J.P. acknowledges support from the Environmental Defense Fund. C.T.R. acknowledges support from the United States Department of Energy and the Grantham Foundation for the Environment.

# References

Amundson, R., L. Stern, T. Baisden, and Y. Wang (1998). The isotopic composition of soil and soil-respired $CO_2$. *Geoderma 82*(1–3), 83–114.

Ancona, F. and A. Marson (2001). A note on the riemann problem for general n×n conservation laws. *Journal of Mathematical Analysis and Applications 260*(1), 279–293.

Appelo, C. A. J. (1996). Multicomponent ion exchange and chromatography in natural systems. In P. C. Lichtner, C. I. Steefel, and E. H. Oelkers (Eds.), *Reactive Transport in Porous Media*, Volume 34 of *Reviews in Mineralogy*, pp. 193–227. Mineralogical Society of America.

Archer, D. (2005). Fate of fossil fuel $CO_2$ in geologic time. *Journal of Geophysical Research: Oceans 110*(C9), C09S05.

Archer, D., H. Kheshgi, and E. Maier-Reimer (1997). Multiple timescales for neutralization of fossil fuel $CO_2$. *Geophysical Research Letters 24*(4), 405–408.

Bear, J. (1972). *Dynamics of Fluids in Porous Media*. New York: American Elsevier.

Beerling, D. J., D. Z. Epihov, I. B. Kantola, M. D. Masters, T. Reershemius, N. J. Planavsky, C. T. Reinhard, J. S. Jordan, S. J. Thorne, J. Weber, M. V. Martin, R. P. Freckleton, S. E. Hartley, R. H. James, C. R. Pearce, E. H. DeLucia, and S. A. Banwart (2024). Enhanced weathering in the US Corn Belt delivers carbon removal with agronomic benefits. *Proceedings of the National Academy of Sciences 121*(9), e2319436121.

Beerling, D. J., E. P. Kantzas, M. R. Lomas, P. Wade, R. M. Eufrasio, P. Renforth, B. Sarkar, M. G. Andrews, R. H. James, C. R. Pearce, J.-F. Mercure, H. Pollitt, P. B. Holden, N. R. Edwards, M. Khanna, L. Koh, S. Quegan, N. F. Pidgeon, I. A. Janssens, J. Hansen, and S. A. Banwart (2020). Potential for large-scale $CO_2$ removal via enhanced rock weathering with croplands. *Nature 583*(7815), 242–248.

Bijma, J., M. Hagens, J. S. Hammes, N. Planavsky, P. A. E. Pogge von Strandmann, T. Reershemius, C. T. Reinhard, P. Renforth, T. J. Suhrhoff, S. Vicca, A. Vienne, and D. Wolf-Gladrow (2026). Reviews and syntheses: Carbon vs. cation based MRV of Enhanced Rock Weathering and the issue of soil organic carbon. *Biogeosciences 23*(1), 53–75.

Blowes, D. W., C. J. Ptacek, and J. L. Jambor (1994). Remediation and prevention of low-quality drainage from tailings impoundments. *Environmental Geochemistry of Sulfide Mine-Wastes 22*, 365–379. Mineralogical Association of Canada Short Course Handbook.

Cameron, M. and J. J. Papike (1981). Structural and chemical variations in pyroxenes. *American Mineralogist 66*(1–2), 1–50.

Cerling, T. E. (1984). The stable isotopic composition of modern soil carbonate and its relationship to climate. *Earth and Planetary Science Letters 71*(2), 229–240.

Charbeneau, R. J. (1988a). Multicomponent exchange and subsurface solute transport: Characteristics, coherence, and the riemann problem. *Water Resources Research 24*(1), 57–64.

Charbeneau, R. J. (1988b). Multicomponent exchange and subsurface solute transport: Characteristics, coherence, and the Riemann problem. *Water Resources Research 24*(1), 57–64.

Clarkson, M. O., C. S. Larkin, P. Swoboda, T. Reershemius, T. J. Suhrhoff, C. N. Maesano, and J. S. Campbell (2024). A review of measurement for quantification of carbon dioxide removal by enhanced weathering in soil. *Frontiers in Climate 6*, 1345224.

Dafermos, C. M. (2005). *Hyperbolic Conservation Laws in Continuum Physics* (2nd ed.). Berlin: Springer.

Dellinger, M., J. Gaillardet, J. Bouchez, D. Calmels, P. Louvat, A. Dosseto, C. Gorge, L. Alanoca, and L. Maurice (2015). Riverine Li isotope fractionation in the Amazon River basin controlled by the weathering regimes. *Geochimica et Cosmochimica Acta 164*, 71–93.

Drever, J. I. (1997). *The Geochemistry of Natural Waters: Surface and Groundwater Environments* (3rd ed.). Upper Saddle River, NJ: Prentice Hall.

Dzombak, D. A. and F. M. M. Morel (1990). *Surface Complexation Modeling: Hydrous Ferric Oxide*. New York: John Wiley & Sons.

Fuss, S., W. F. Lamb, M. W. Callaghan, J. Hilaire, F. Creutzig, T. Amann, T. Beringer, W. de Oliveira Garcia, J. Hartmann, T. Khanna, G. Luderer, G. F. Nemet, J. Rogelj, P. Smith, J. L. V. Vicente, J. Wilcox, M. del Mar Zamora Dominguez, and J. C. Minx (2018). Negative emissions—Part 2: Costs, potentials and side effects. *Environmental Research Letters 13*(6), 063002.

Guo, F., H. Sun, J. Yang, L. Zhang, Y. Mu, Y. Wang, and F. Wu (2023). Improving food security and farmland carbon sequestration in China through enhanced rock weathering: Field evidence and potential assessment in different humid regions. *Science of The Total Environment 903*, 166118.

Hamilton, S. K., A. L. Kurzman, C. Arango, L. Jin, and G. P. Robertson (2007). Evidence for carbon sequestration by agricultural liming. *Global Biogeochemical Cycles 21*(2), GB2021.

Hammes, J. S., J. Hartmann, J. A. C. Barth, T. Linke, I. Smet, M. Hagens, P. A. E. Pogge von Strandmann, T. Reershemius, B. Casimiro, A. Vienne, A. A. Stoeckel, R. Steffens, and D. Paessler (2025). Soil processes govern alkalinity and cation retention in enhanced weathering for carbon dioxide removal. *EGUsphere*. Preprint.

Hartmann, J., A. J. West, P. Renforth, P. Köhler, C. L. De La Rocha, D. A. Wolf-Gladrow, H. H. Dürr, and J. Scheffran (2013). Enhanced chemical weathering as a geoengineering strategy to reduce atmospheric carbon dioxide, supply nutrients, and mitigate ocean acidification. *Reviews of Geophysics 51*(2), 113–149.

Hasemer, H., J. Borevitz, and W. Buss (2024). Measuring enhanced weathering: inorganic carbon-based approaches may be required to complement cation-based approaches. *Frontiers in Climate 6*, 1352825.

Helfferich, F. G. (1993). Multicomponent wave propagation: The coherence principle. An introduction. In D. Petruzzelli and F. G. Helfferich (Eds.), *Migration and Fate of Pollutants in Soils and Subsoils*, Volume 32 of *NATO ASI Series*, pp. 197–232. Berlin: Springer.

Helfferich, F. G. and G. Klein (1970). *Multicomponent Chromatography: Theory of Interference*. New York: Marcel Dekker.

Hindshaw, R. S., R. Tosca, T. L. Goût, I. Farnan, N. J. Tosca, and E. T. Tipper (2019). Experimental constraints on Li isotope fractionation during clay formation. *Geochimica et Cosmochimica Acta 250*, 219–237.

Holden, F. J., K. Davies, M. I. Bird, R. Hume, H. Green, D. J. Beerling, and P. N. Nelson (2024). In-field carbon dioxide removal via weathering of crushed basalt applied to acidic tropical agricultural soil. *Science of the Total Environment 955*, 176568.

IPCC (2022). Climate change 2022: Mitigation of climate change. contribution of working group iii to the sixth assessment report of the intergovernmental panel on climate change. Technical report.

Juanes, R. and T. Patzek (2004). Analytical solution to the riemann problem of three-phase flow in porous media. *TRANSPORT IN POROUS MEDIA 55*(1), 47–70.

Jurjovec, J., C. J. Ptacek, and D. W. Blowes (2002). Acid neutralization mechanisms and metal release in mine tailings: A laboratory column experiment. *Geochimica et Cosmochimica Acta 66*(9), 1511–1523.

Kantzas, E. P., D. J. Beerling, M. R. Lomas, R. M. Eufrasio, P. Renforth, A. L. Lewis, L. L. Taylor, E. J. Sherlock, M. Val Martin, R. H. James, and C. R. Pearce (2025). Transforming US agriculture for carbon removal with enhanced weathering. *Nature*.

Kanzaki, Y., N. J. Planavsky, and C. T. Reinhard (2024). Soil cation storage as a key control on the timescales of carbon dioxide removal through enhanced weathering. *Communications Earth & Environment 5*, 155.

Kelland, M. E., P. W. Wade, A. L. Lewis, L. L. Taylor, B. Mayber, and D. J. Beerling (2020). Increased yield and $CO_2$ sequestration potential with the C4 cereal Sorghum bicolor cultivated in basaltic rock dust-amended agricultural soil. *Global Change Biology 26*(6), 3658–3676.

Khalidy, R. and R. M. Santos (2024). Fate and migration of enhanced rock weathering products through soil horizons; implications of irrigation and percolation regimes. *Geoderma 441*, 116759.

Knapp, R. B. (1989). Spatial and temporal scales of local equilibrium in dynamic fluid-rock systems. *Geochimica et Cosmochimica Acta 53*(8), 1955–1964.

Lake, L., S. Bryant, and A. Araque-Martinez (2002). *Geochemistry and Fluid Flow. 1st edn.* Elsevier, Amsterdam.

Langmuir, I. (1918). The adsorption of gases on plane surfaces of glass, mica and platinum. *Journal of the American Chemical Society 40*(9), 1361–1403.

Lax, P. D. (1957). Hyperbolic systems of conservation laws II. *Communications on Pure and Applied Mathematics 10*(4), 537–566.

LeVeque, R. J. (2002). *Finite Volume Methods for Hyperbolic Problems*. Cambridge University Press.

Liu, T. (1974). Riemann problem for general 2 × 2 conservation laws. *Trans. Am. Math. Soc.* (199), 89–112.

McNeece, C. J. and M. A. Hesse (2016a). Challenges in coupling acidity and salinity transport in porous media. *Advances in Water Resources 97*, 1–17.

McNeece, C. J. and M. A. Hesse (2016b). Reactive transport of aqueous protons in porous media. *Advances in Water Resources 97*, 314–325.

McNeece, C. J., J. Lützenkirchen, and M. A. Hesse (2018). Chromatographic analysis of the acidity-salinity transport system. *Journal of Contaminant Hydrology 216*, 27–37.

Minx, J. C., W. F. Lamb, M. W. Callaghan, S. Fuss, J. Hilaire, F. Creutzig, T. Amann, T. Beringer, W. de Oliveira Garcia, J. Hartmann, T. Khanna, D. Lenzi, G. Luderer, G. F. Nemet, J. Rogelj, P. Smith, J. L. Vicente Vicente, J. Wilcox, and M. del Mar Zamora Dominguez (2018). Negative emissions—Part 1: Research landscape and synthesis. *Environmental Research Letters 13*(6), 063001.

National Academies of Sciences, Engineering, and Medicine (2019). *Negative Emissions Technologies and Reliable Sequestration: A Research Agenda*. Washington, DC: The National Academies Press.

Nordstrom, D. K. (2011). Mine waters: Acidic to circumneutral. *Elements 7*(6), 393–398.

Perez-Fodich, A. and L. A. Derry (2019). Organic acids and high soil $CO_2$ drive intense chemical weathering of Hawaiian basalts: Insights from reactive transport models. *Geochimica et Cosmochimica Acta 249*, 173–198.

Pistiner, J. S. and G. M. Henderson (2003). Lithium-isotope fractionation during continental weathering processes. *Earth and Planetary Science Letters 214*(1–2), 327–339.

Pogge von Strandmann, P. A. E., P. J. Frings, and M. J. Murphy (2017). Lithium isotope behaviour during weathering in the Ganges Alluvial Plain. *Geochimica et Cosmochimica Acta 198*, 17–31.

Pogge von Strandmann, P. A. E., S. A. Kasemann, and J. B. Wimpenny (2020). Lithium and lithium isotopes in Earth's surface cycles. *Elements 16*(4), 253–258.

Prigiobbe, V., M. A. Hesse, and S. L. Bryant (2012a). Anomalous reactive transport in the framework of the theory of chromatography. *TRANSPORT IN POROUS MEDIA 93*(1), 127–145.

Prigiobbe, V., M. A. Hesse, and S. L. Bryant (2012b). Fast strontium transport induced by hydrodynamic dispersion and ph-dependent sorption. *Geophysical Research Letters 39*(18).

Prigiobbe, V., M. A. Hesse, and S. L. Bryant (2013a). Anomalous reactive transport in the framework of the theory of chromatography. *Transport in Porous Media 97*(1), 97–141.

Prigiobbe, V., M. A. Hesse, and S. L. Bryant (2013b). Hyperbolic theory for flow in permeable media with ph-dependent adsorption. *SIAM Journal on Applied Mathematics 73*(5), 1941–1957.

Rahnemaie, R., T. Hiemstra, and W. H. van Riemsdijk (2006a). Inner- and outer-sphere complexation of ions at the goethite-solution interface. *Journal of Colloid and Interface Science 297*(2), 379–388.

Rahnemaie, R., T. Hiemstra, and W. H. van Riemsdijk (2006b). A new surface structural approach to ion adsorption: Tracing the location of electrolyte ions. *Journal of Colloid and Interface Science 293*(2), 312–321.

Reershemius, T., M. E. Kelland, J. S. Jordan, I. R. Davis, R. D'Ascanio, B. Kalderon-Asael, D. Asael, T. J. Suhrhoff, D. Z. Epihov, D. J. Beerling, C. T. Reinhard, and N. J. Planavsky (2023). Initial validation of a soil-based mass-balance approach for empirical monitoring of enhanced rock weathering rates. *Environmental Science & Technology 57*(48), 19497–19507.

Renforth, P. and G. Henderson (2017). Assessing ocean alkalinity for carbon sequestration. *Reviews of Geophysics 55*(3), 636–674.

Renforth, P., P. A. E. P. von Strandmann, and G. M. Henderson (2015). The dissolution of olivine added to soil: Transport experiments and an initial model. *Applied Geochemistry 61*, 109–118.

Rhee, H., A. Aris, and N. Amudson (1989). *First-Order Partial Differential Equations, Theory and Application of Hyperbolic Systems of Quasilinear Equations. Vol. II,*. Prentice-Hall, Englewood Cliffs, NJ, USA.

Rhee, H.-K. and N. R. Amundson (1972). A study of the shock layer in nonequilibrium exchange systems. *Chemical Engineering Science 27*(2), 199–211.

Skov, K., J. Wardman, M. Healey, A. McBride, T. Bierowiec, J. Cooper, I. Edeh, D. George, M. E. Kelland, J. Mann, D. Manning, M. J. Murphy, R. Pape, Y. A. Teh, W. Turner, P. Wade, and X. Liu (2024). Initial agronomic benefits of enhanced weathering using basalt: A study of spring oat in a temperate climate. *PLOS ONE 19*(3), e0295031.

Smoller, J. (1994). *Shock Waves and Reaction-Diffusion Equations* (2nd ed.). New York: Springer.

Sposito, G. (2004). *The Surface chemistry of natural particles*. Oxford University Press, New York, NY, USA.

Sposito, G. (2008a). *The Chemistry of Soils* (2nd ed.). New York: Oxford University Press.

Sposito, G. (2008b). *Chemistry of soils, II Ed.* Oxford University Press, New York, NY, USA.

Steefel, C. I. and A. C. Lasaga (1994). A coupled model for transport of multiple chemical species and kinetic precipitation/dissolution reactions with application to reactive flow in single phase hydrothermal systems. *American Journal of Science 294*(5), 529–592.

Strefler, J., T. Amann, N. Bauer, E. Kriegler, and J. Hartmann (2018). Potential and costs of carbon dioxide removal by enhanced weathering of rocks. *Environmental Research Letters 13*(3), 034010.

Stumm, W. and J. J. Morgan (1996a). *Aquatic Chemistry: Chemical Equilibria and Rates in Natural Waters* (3rd ed.). New York: John Wiley & Sons.

Stumm, W. and J. J. Morgan (1996b). *Aquatic Chemistry: Chemical Equilibria and Rates in Natural Waters* (3rd ed.). New York: John Wiley & Sons.

Suhrhoff, T. J., T. Reershemius, J. Wang, J. S. Jordan, C. T. Reinhard, and N. J. Planavsky (2024). A tool for assessing the sensitivity of soil-based approaches for quantifying enhanced weathering: A US case study. *Frontiers in Climate 6*, 1346117.

Taylor, L. L., C. T. Driscoll, P. M. Groffman, G. H. Rau, J. D. Blum, and D. J. Beerling (2021). Increased carbon capture by a silicate-treated forested watershed affected by acid deposition. *Biogeosciences 18*(1), 169–188.

te Pas, E. E. E. M., E. Chang, A. R. Marklein, R. N. J. Comans, and M. Hagens (2024). Accounting for retarded weathering products in comparing methods for quantifying carbon dioxide removal in a short-term enhanced weathering study. *Frontiers in Climate 6*, 1524998.

Temple, B. (1983). Systems of conservation laws with coinciding shock and rarefaction curves. *Contemporary Mathematics, 17*, 143–151.

Tipper, E. T., A. Galy, J. Gaillardet, M. J. Bickle, H. Elderfield, and E. A. Carder (2006). The magnesium isotope budget of the modern ocean: Constraints from riverine magnesium isotope ratios. *Earth and Planetary Science Letters 250*(1–2), 241–253.

Valocchi, A. J., R. L. Street, and P. V. Roberts (1981). Transport of ion-exchanging solutes in groundwater: Chromatographic theory and field simulation. *Water Resources Research 17*(5), 1517–1527.

van Beinum, W., A. Hofmann, J. C. L. Meeussen, and R. Kretzschmar (2005). Sorption kinetics of strontium in porous hydrous ferric oxide aggregates I. The Donnan diffusion model. *Journal of Colloid and Interface Science 283*(1), 18–28.

Venkatraman, A., M. A. Hesse, L. W. Lake, and R. T. Johns (2014). Analytical solutions for flow in porous media with multicomponent cation exchange reactions. *Water Resources Research 50*(7), 5831–5847.

Vicca, S., D. S. Goll, M. Hagens, J. Hartmann, I. A. Janssens, A. Neubeck, J. Peñuelas, S. Poblador, J. Rijnders, J. Sardans, E. Struyf, P. Swoboda, J. W. van Groenigen, A. Vienne, and E. Verbruggen (2022). Is the climate change mitigation effect of enhanced silicate weathering governed by biological processes? *Global Change Biology 28*(3), 711–726.

Vienne, A., S. Poblador, M. Portillo-Estrada, J. Hartmann, S. Ijiehon, P. Wade, and S. Vicca (2022). Enhanced weathering using basalt rock powder: Carbon sequestration, co-benefits and risks in a mesocosm study with *Solanum tuberosum*. *Frontiers in Climate 4*, 869456.

Ziegler, K., O. A. Chadwick, M. A. Brzezinski, and E. F. Kelly (2005). Natural variations of $\delta^{30}$Si ratios during progressive basalt weathering, Hawaiian Islands. *Geochimica et Cosmochimica Acta 69*(19), 4597–4610.

# A Derivation of solute transport equation in a simple porous medium

The conservation of solute mass is used to derive equations for solute transport along a porous column of soil. A unidirectional flow is assumed so that the variation in solute concentration in the spanwise direction is small relative to the variation in the streamwise direction. The dissolved solutes are denoted $c_i$ where $i$ can be any species of dissolved solute (e.g. $\mathrm{Ca}^{2+}$, $\mathrm{Mg}^{2+}$, $\mathrm{H}^{+}$). The concentration of any solute $i$ adsorbed on the surface of the soil grains comprising the porous medium, defined as loading $z_i$, is assumed to be motionless. The concentration of solutes in the fluid phase and adsorbed onto charged surfaces affects the equilibrium behavior of adsorption.

The evolution equation for the dissolved solute is given by

$$A\frac{\partial \phi c_i}{\partial t} + \frac{\partial}{\partial x}\left[A\mathcal{J}_i\right] = Sf([c_1, c_2, \ldots, c_N], [z_1, z_2, \ldots, z_N]), \tag{A.1}$$

where $\mathcal{J}_i$ is the net mass flux of solute $i$, and $\phi$ represents the porosity (void volume per volume of medium). Further, the Jacobians of the cross-sectional area with the normal pointing towards $x$-direction and the volume are represented as $A$ and $S$, respectively. The reaction term, $f$, describes the exchange of components between phases via adsorption. We assume that the cross-sectional geometry (area) of the water flow remains constant, so Equation (A.2) becomes

$$\frac{\partial \phi c_i}{\partial t} + \frac{\partial}{\partial x}\mathcal{J}_i = \gamma f([c_1, c_2, \ldots, c_N], [z_1, z_2, \ldots, z_N]), \tag{A.2}$$

with the shape factor $\gamma = S/A$ (units of inverse length scale), equivalent to the inverse of the hydraulic radius. If the flowpath is a wide rectangular section, then $\gamma = 1/H$ whereas for a cylindrical furrow flowing half-full $H = r$, $\gamma = 2/r$ where $r$ is the radius of the cylinder.

Next, the mass flux $\mathcal{J}_i$ for the solute $i$ is defined

$$\mathcal{J}_i \coloneqq q c_i - \phi D \frac{\partial}{\partial x} c_i, \tag{A.3}$$

where $D = D_m + D_{hd}$, is the combination of molecular diffusion and hydrodynamic dispersion of the solute in the fluid phase and $q$ is the Darcy flux of water in the pore fluid, $q = \phi(x,t)v(x,t)$ with $v$ being the interstitial velocity of water. We define $\mathit{\Gamma}_i = \gamma f([c_1, c_2, \ldots, c_N], [z_1, z_2, \ldots, z_N])$ and combine Equations (A.2) and (A.3) to obtain a dimensional solute evolution equation.

$$\frac{\partial \phi c_i}{\partial t} + \frac{\partial}{\partial x}\left[q c_i - \phi D \frac{\partial}{\partial x} c_i\right] = -\mathit{\Gamma}_i, \tag{A.4}$$

where the term $\mathit{\Gamma}$ represents the mass transfer of solute from the fluid phase to the solid phase (i.e. soil) due to adsorption.

## B Dimensional loading isosurfaces

We begin our ERW focused case study by taking Equations (8)—(11) and explicitly specifying that species $i \in \{\mathrm{Ca}^{2+}, \mathrm{Mg}^{2+}, \mathrm{H}^{+}\}$ so

$$z_{\mathrm{Ca}} = \varphi\left(\frac{c_{\mathrm{Ca}} K_{\mathrm{Ca}} Z_t}{1 + c_{\mathrm{H}} K_{\mathrm{H}} + c_{\mathrm{Ca}} K_{\mathrm{Ca}} + c_{\mathrm{Mg}} K_{\mathrm{Mg}}}\right), \tag{B.1a}$$

$$z_{\mathrm{Mg}} = \varphi\left(\frac{c_{\mathrm{Mg}} K_{\mathrm{Mg}} Z_t}{1 + c_{\mathrm{H}} K_{\mathrm{H}} + c_{\mathrm{Ca}} K_{\mathrm{Ca}} + c_{\mathrm{Mg}} K_{\mathrm{Mg}}}\right), \tag{B.1b}$$

$$z_{\mathrm{H}} = \varphi\left(\frac{c_{\mathrm{H}} K_{\mathrm{H}} Z_t}{1 + c_{\mathrm{H}} K_{\mathrm{H}} + c_{\mathrm{Ca}} K_{\mathrm{Ca}} + c_{\mathrm{Mg}} K_{\mathrm{Mg}}}\right). \tag{B.1c}$$

where

$$Z_t = \left[\mathrm{X}^{-1/2}\right] + \left[\mathrm{XH}^{1/2}\right] + \left[\mathrm{XCa}^{3/2}\right] + \left[\mathrm{XMg}^{3/2}\right]. \tag{B.2}$$

We note here that the expression

$$\varphi = \frac{\phi}{1-\phi} \tag{B.3}$$

is a constant for this treatment of simple porous media so we absorb the porosity factor in the the adsorption gradient.

# C Dimensionless equations for solute transport with competitive solute adsorption

The full dimensionless problem statement using the kinetic formulation at constant fluid flux and porosity, $\bar{q} = \phi\bar{v}$, and constant diffusivity, $D = D^*$, is

$$\frac{\partial \phi c_i}{\partial t} + \frac{\partial \phi c_i}{\partial x} - \phi \mathrm{Pe}^{-1}\left(\frac{\partial^2 c}{\partial x^2}\right) = -\mathrm{Da}\ \Gamma, \quad x \in \mathbb{R},\ t > 0, \tag{C.1a}$$

$$(1-\phi)\frac{\partial z_i}{\partial t} = \mathrm{Da}\ \Gamma, \qquad x \in \mathbb{R},\ t > 0, \tag{C.1b}$$

$$z_i^{eq} = f(\mathbf{c}^{eq}, \mathbf{z}^{eq}), \tag{C.1c}$$

$$c_i(x,0) = c_i^0(x). \tag{C.1d}$$

where $\mathbf{c}^{eq} = [c^{eq}_{\mathrm{Ca}}, c^{eq}_{\mathrm{Mg}}]$, and $\mathbf{z}^{eq} = [z^{eq}_{\mathrm{Ca}}, z^{eq}_{\mathrm{Mg}}]$ At local equilibrium $z_i = z_i^{eq}$ and $c_i = c_i^{eq}$. By adding Equations (C.1a) and (C.1b) together we can thus retrieve a single equation for total solute conservation at equilibrium conditions, thereby eliminating the $\mathrm{Da}{\cdot}\Gamma$ terms in (C.1a) and (C.1b). At constant porosity, the mass balance equation is written

$$\frac{\partial}{\partial t}\left(c_i^{eq} + \varphi z_i^{eq}\right) + \frac{\partial c_i^{eq}}{\partial x} - \mathrm{Pe}^{-1}\left(\frac{\partial^2 c_i^{eq}}{\partial x^2}\right) = 0. \tag{C.2}$$

Now it is worth noting that $\mathbf{z}^{eq}$ may be generically rewritten as a function of $\mathbf{c}^{eq}$ as stated in equation (C.1c).